DEPARTMENT OF MECHANICAL ENGINEERING AND MECHANICS
COLLEGE OF ENGINEERING AND TECHNOLOGY
OLD DOMINION UNIVERSITY
NORFOLK, VIRGINIA 23529

ANALYSIS AND MITIGATION OF NUMERICAL DISSIPATION IN INVISCID AND VISCID COMPUTATION OF VORTEX-DOMINATED FLOWS

By

Osama A. Kandil, principal investigator

Final Report
For the period February 1988 to November 1988

Prepared for
National Aeronautics and Space Administration
Langley Research Center
Hampton, Virginia 23665

Under
NASA Research Grant NAG-1-846
Dr. C.-H. Liu, Technical Monitor
FLDMD-Theoretical Flow Physics Branch

Submitted by the
Old Dominion University Research Foundation
P.O. Box 6369
Norfolk, Virginia 23508-0369

August 1990

ANALYSIS AND MITIGATION OF NUMERICAL DISSIPATION IN INVISCID AND VISCID COMPUTATION OF VORTEX-DOMINATED FLOWS

Osama A. Kandil

Accomplishments

In the period of February 1988 to November 1988, The Principal Investigator with the assistance of one of his Ph.D. Students has achieved the following accomplishments:

1. **Publication: Kandil, O.A. and Chuang, H. A., "Unsteady Delta-Wing Flow Computation Using An Implicit Factored Euler Scheme," AIAA 88–3649–CP, AIAA/ASME/SIAM/APS 1st National Fluid Dynamics Congress, Cincinnati, Ohio, July 25–28, 1988, pp. 248–255. A copy of the paper is attached.**

Abstract

The conservative unsteady Euler equations for the flow relative motion in the moving frame of reference are used to solve for the steady and unsteady flows around sharp-edged delta wings. The resulting equations are solved by using an implicit approximately-factored finite-volume scheme. Implicit second-order and explicit second- and fourth-order dissipations are added to the scheme. The boundary conditions are explicitly satisfied. The grid is generated by locally using a modified Joukowski transformation in cross-flow planes at the grid chord stations. The computational applications cover a steady flow around a delta wing whose results serve as the initial conditions for the unsteady flow around a pitching delta wing about a large angle of attack. The steady results are compared with the experimental data and the periodic solution is achieved within the third cycle of oscillation.

2. **Journal Publication: Kandil, O. A. and Chuang, H. A., "Computation of Vortex-Dominated Flow for a Delta Wing Undergoing Pitching Oscillation," AIAA Journal, Vol. 28, No. 9, September 1990. A copy of the manuscript is attached.**

3. **Publication: Wong, T. C., Kandil, O. A. and Liu, C. H., "Navier-Stokes Computations of Separated Vortical Flows Past Prolate Spheroid at Incidence," AIAA Paper No. 89–0553, Reno, Nevada, January 9–12, 1990.**

Abstract

The problem of steady incompressible viscous flow past prolate spheroids at incidence is formulated using the unsteady incompressible thin-layer Navier-Stokes (NS) equations and the unsteady compressible thin-layer Navier-Stokes equations. For the incompressible equations, a

certain level of unsteady artificial compressibility is added to the continuity equation to secure the coupling with the momentum equations during the psuedo-time stepping. The two sets of Navier-Stokes equations are solved using a psuedo-time stepping of the implicit flux-difference splitting scheme on a curvilinear grid, which is generated by a transfinite grid generator. The Baldwin and Lomax algebraic eddy viscosity model is used to model the turbulent flow. The computational applications cover a 6:1 prolate spheroid at different angles of attack and different Reynolds number. The results are compared with the experimental data.

AIAA'88

AIAA-88-3649-CP
Unsteady Delta-Wing Flow Computation Using an Implicit Factored Euler Scheme

Osama A. Kandil and H. Andrew Chuang, Department of Mechanical Engineering and Mechanics, Old Dominion Univ., Norfolk, VA

AIAA/ASME/SIAM/APS
1st National Fluid Dynamics Congress
July 25-28, 1988/Cincinnati, Ohio

UNSTEADY DELTA-WING FLOW COMPUTATION USING AN IMPLICIT FACTORED EULER SCHEME

88-3649-CP

Osama A Kandil* and H. Andrew Chuang**
Department of Mechanical Engineering and Mechanics
Old Dominion University, Norfolk, VA 23529-0247

Abstract

The conservative unsteady Euler equations for the flow relative motion in the moving frame of reference are used to solve for the steady and unsteady flows around sharp-edged delta wings. The resulting equations are solved by using an implicit approximately-factored finite-volume scheme. Implicit second-order and explicit second- and fourth-order dissipations are added to the scheme. The boundary conditions are explicitly satisfied. The grid is generated by locally using a modified Joukowski transformation in cross-flow planes at the grid chord stations. The computational applications cover a steady flow around a delta wing whose results serve as the initial conditions for the unsteady flow around a pitching delta wing about a large angle of attack. The steady results are compared with the experimental data and the periodic solution is achieved within the third cycle of oscillation.

Introduction

Unsteady flows around delta wings are characterized by the existence of unsteady large- and small-scale vortices (primary, secondary and possible tretiary vortices), moving shock waves with time-dependent strengths, time-dependent vortex-core formation and breakdown (bubble and spiral-vortex breakdown), and interaction of shock waves with the vortical-region and the surface-boundary-layer flows. These highly unsteady aerodynamic loads may interact with the wing structural response causing aeroelastic instabilities which may restrict the aircraft flight envelope. In Ref. 1, the status of computational unsteady aerodynamics for aeroelastic analysis has been discussed, and recommendations for future code development for separated and vortex-dominated flows are presented.

The literature on the computational solution and experimental data of the unsteady vortex-dominated flows, particularly in the transonic regime, is unfortunately very limited. This is attributed to the complexity of the flow and its dependence on numerous parameters, and the substantial computational cost involved for the flow resolution and the time-accurate computations.

Most of the existing unsteady computational schemes are based on the unsteady small disturbance (UTSD) theory[2-4], unsteady full potential (UFP) equation[5-7], UTSD equation with non-isentropic flow corrections[8] and UFP equation with non-isentropic flow corrections[9]. These schemes are restricted to attached flows only. For mildly separated flows, integral and finite-difference boundary-layer schemes have been coupled with potential flow schemes[10,11].

The unsteady Euler equations adequately model shock waves and their motion, entropy increase across shocks and entropy gradient and vorticity production and convection behind shocks, as can be seen from Crocco's theorem and the inviscid vorticity transport equation. Moreover, the computational solution of Euler equations adequately models separated flow from sharp edges[12-14]. For smooth-surface separation, round-edge separation, shock-induced separation, viscous diffusion and dissipation, vortex breakdown, flow transition and turbulence; viscous terms must be added to Euler equations to recover the full Navier-Stokes equations or an approximate form of these equations. Although the process of adding the viscous terms to the unsteady Euler solvers is simple and straightforward, the computational cost for high-Reynolds-number unsteady flows is substantial and might be prohibitive due to the need for fine grids to adequately resolve the viscous effects.

Euler/Navier-Stokes zonal approaches[15,16] have been demonstrated to maintain the accuracy of the Navier-Stokes solutions and in the meantime, alleviate to a good extent the computational cost of the Navier-Stokes equations. These approaches along with fine grids embedding in the vortical regions should be developed further for unsteady flows.

Recently, successful time accurate solutions of the unsteady Euler and Navier-Stokess equations have been presented for airfoils[14,17-20]. The only existing unsteady Euler solutions for vortex-dominated flows are those of the rolling-oscillation of a sharp-edge delta wing in a locally conical supersonic flow around a mean angle of attack and a zero angle of attack, which were presented by the authors in Refs. 13 and 14. The authors derived the unsteady Euler equations for the flow relative motion in a moving frame of reference, and the equations have been solved by using an explicit, multi-stage time stepping, finite-volumn scheme. Periodic solutions were achieved in the third cycle of rolling oscillation. Details of the surface pressure, cross-flow velocity and cross-flow Mach contours were presented showing the primary vortex and wave

*Professor, Associate Fellow AIAA.

**Graduate Research Assistant, Member AIAA.

shocks formation and interaction.

In the present paper, the three-dimensional unsteady Euler equations in a moving frame of reference are solved by using an implicit approximately-factored finite-volume scheme. The unsteady airfoil computations of this scheme were compared earlier with the experimental data of ref. 21, which were in good agreement. The present three-dimensional steady results are compared with the experimental data of ref. 22 for two levels of explicit dissipation. With the steady results serving as initial conditions for the unsteady flow, the flow around the same delta wing undergoing pitching oscillation about the quarter-chord axis is solved in this paper.

Formulation

Starting with the conservative form of the unsteady Euler equations for the flow absolute motion in the space-fixed frame of reference, and using the following relations for the substantial and local derivatives of a scalar "a" and a vector "$\bar{A}$"

$$\frac{Da}{Dt} = \frac{D'a}{Dt'} \tag{1.a}$$

$$\frac{\partial a}{\partial t} = \frac{\partial' a}{\partial t'} - \bar{V}_t \cdot \nabla a \tag{1.b}$$

$$\frac{D\bar{A}}{Dt} = \frac{D'\bar{A}}{Dt'} + \bar{\omega}\times\bar{A} \tag{1.c}$$

$$\frac{\partial \bar{A}}{\partial t} = \frac{\partial' \bar{A}}{\partial t'} - \bar{V}_t \cdot \nabla\bar{A} + \bar{\omega}\times\bar{A} \tag{1.d}$$

we obtain the conservative unsteady Euler equations for the flow relative motion in the moving-frame of reference. In terms of the Cartesian coordinates x', y', z' of the moving-frame of reference, the resulting Euler equations are

$$\frac{\partial' \bar{q}_r}{\partial t'} + \frac{\partial' \bar{E}_r}{\partial x'} + \frac{\partial' \bar{F}_r}{\partial y'} + \frac{\partial' \bar{G}_r}{\partial z'} = \bar{S} \tag{2}$$

where

$$\bar{q}_r = [\rho,\ \rho u_r,\ \rho v_r,\ \rho w_r,\ \rho e_r]^t \tag{3}$$

$$\bar{E}_r = [\rho u_r,\ \rho u_r^2 + p,\ \rho u_r v_r,\ \rho u_r w_r,\ \rho u_r h_r]^t \tag{4}$$

$$\bar{F}_r = [\rho v_r,\ \rho u_r v_r,\ \rho v_r^2 + p,\ \rho v_r w_r,\ \rho v_r h_r]^t \tag{5}$$

$$\bar{G}_r = [\rho w_r,\ \rho u_r w_r,\ \rho v_r w_r,\ \rho w_r^2 + p,\ \rho w_r h_r]^t \tag{6}$$

$$\bar{S} = [0,\ -\rho a_{tx'},\ -\rho a_{ty'},\ -\rho a_{tz'},\ -\rho[\bar{V}_r \cdot \bar{a}_o + (\bar{\omega}\times\bar{r}) \cdot \bar{a}_o + \bar{V}_o \cdot (\bar{a}_t - \bar{\omega}\times\bar{V}_r) + \bar{V}_r \cdot (\bar{\omega}\times\bar{r}) + (\bar{\omega}\times\bar{r}) \cdot (\bar{\omega}\times\bar{r})]]^t \tag{7}$$

$$e_r = e - \bar{V} \cdot \bar{V}_t = \frac{p}{\rho(\gamma-1)} + \frac{V_r^2}{2} - \frac{V_t^2}{2} \tag{8}$$

$$h_r = h - \bar{V} \cdot \bar{V}_t = \frac{\gamma p}{\rho(\gamma-1)} + \frac{V_r^2}{2} - \frac{V_t^2}{2} \tag{9}$$

$$\bar{V}_t = \bar{V} - \bar{V}_r = \bar{V}_o + \bar{\omega} \times \bar{r} \tag{10}$$

$$\bar{a}_t = \bar{a} - \bar{a}_r = \frac{D\bar{V}}{Dt} - \frac{D'\bar{V}_r}{Dt'} = \dot{\bar{a}}_o + \dot{\bar{\omega}} \times \bar{r} + 2\bar{\omega} \times \bar{V}_r + \bar{\omega} \times (\bar{\omega} \times \bar{r}) \tag{11}$$

$$\bar{\omega} = \omega_{x'}\hat{i} + \omega_{y'}\hat{j} + \omega_{z'}\hat{k} = (-\dot{\alpha}\sin\beta + \dot{\theta})\,\hat{i} + (\dot{\alpha}\cos\beta\sin\theta + \dot{\beta}\cos\theta)\,\hat{j} + (\dot{\alpha}\cos\beta\cos\theta - \dot{\beta}\sin\theta)\,\hat{k} \tag{12}$$

In Eqs. (1)-(12), $\bar{q}_r$ is the flow vector field of relative motion; $\bar{E}_r$, $\bar{F}_r$ and $\bar{G}_r$ the inviscid fluxes of the relative motion, $\bar{S}$ a source term due to the motion of the reference frame, ρ the density, p the pressure, e and h the total energy and total enthalpy per unit mass, $\bar{V}$ and $\bar{a}$ the flow absolute velocity and absolute acceleration, $\bar{V}_r$ and $\bar{a}_r$ the flow relative velocity and relative acceleration, $\bar{V}_t$ and $\bar{a}_t$ the transformation velocity and transformation acceleration, $\bar{V}_o$ and $\bar{a}_o$ the translation velocity and translation acceleration of the moving frame, $\bar{\omega}$ and $\dot{\bar{\omega}}$ the angular velocity and angular acceleration of the moving frame, $\bar{r}$ the position vector of a fluid particle with respect to the moving frame, and γ is the ratio of specific heats. The pitch, yaw and roll angles are referred to by using the Eulerian angles α, β and θ; respectivley. The "'" refers to the derivatives, time or coordinates with respect to the moving frame of reference.

Introducing the curvilinear coordinates ξ', η' and ζ' in the moving frame of reference, which are given by

$$\xi' = \xi'(x',y',z'),\ \eta' = \eta'(x',y',z'),$$

$$\zeta' = \zeta'(x', y', z') \tag{13}$$

Eqs. (2)-(7) are transformed to

$$\frac{\partial' \hat{Q}_r}{\partial t'} + \frac{\partial' \hat{E}_r}{\partial \xi'} + \frac{\partial' \hat{F}_r}{\partial \eta'} + \frac{\partial' \hat{G}_r}{\partial \zeta'} = \hat{S} \tag{14}$$

$$\hat{Q}_r = J^{-1} [\rho,\ \rho u_r,\ \rho v_r,\ \rho w_r,\ \rho e_r]^t \tag{15}$$

$$\hat{E}_r = J^{-1} [\rho U_r,\ \rho u_r U_r + \xi_x' p,\ \rho v_r U_r + \xi_y' p,$$

$$\rho w_r U_r + \xi_z' p,\ \rho U_r h_r]^t \tag{16}$$

$$\hat{F}_r = J^{-1} [\rho V_r,\ \rho u_r V_r + \eta_x' p,\ \rho v_r V_r + \eta_y' p,$$

$$\rho w_r V_r + \eta_z' p,\ \rho V_r h_r]^t \tag{17}$$

$$\hat{G}_r = J^{-1} [\rho W_r,\ \rho u_r W_r + \zeta_x' p,\ \rho v_r W_r + \zeta_y' p,$$

$$\rho w_r W_r + \zeta_z' p,\ \rho W_r h_r]^t \tag{18}$$

$$\hat{S} = J^{-1} \bar{S} \tag{19}$$

In Eqs. (15)-(19), J^{-1} is the Jacobian of transformation and U_r, V_r and W_r are the contravariant velocity components.

Computational Scheme

Equation (14) is integrated over ξ', η' and ζ' the divergence theorem is applied to the resulting equation. By using the implicit approximate factorization scheme, we obtain the following difference equation for a typical cell (i, j, k)

$$\left[\frac{I}{J\Delta t'} + \delta_{\xi'} A_r^n - \frac{H_r^n}{J} - D_{m\xi'}\right] \times$$

$$\left[\frac{I}{J\Delta t'} + \delta_{\eta'} B_r^n - D_{m\eta'}\right] \times$$

$$\left[\frac{I}{J\Delta t'} + \delta_{\zeta'} C_r^n - D_{m\zeta'}\right] \Delta \bar{q}_r^n = -\frac{1}{(J\Delta t')^2} \bar{W}(\bar{q}_r^n) \tag{20}$$

where

$$\bar{W}(\bar{q}_r^n) = (\hat{E}^n_{r_{i+1/2,j,k}} - \hat{E}^n_{r_{i-1/2,j,k}})$$

$$+ (\hat{F}^n_{r_{i,j+1/2,k}} - \hat{F}^n_{r_{i,j-1/2,k}})$$

$$+ (\hat{G}^n_{r_{i,j,k+1/2}} - \hat{G}^n_{r_{i,j,k-1/2}})$$

$$- \hat{S}^n_{i,j,k} - D_{e\xi'}(\bar{q}_r^n)$$

$$- D_{e\eta'}(\bar{q}_r^n) - D_{e\zeta'}(\bar{q}_r^n) \tag{21}$$

In Eqs. (20) and (21), A_r, B_r, C_r and H_r are the Jacobian matrices $\partial \hat{E}_r / \partial \bar{q}_r$, $\partial \hat{F}_r / \partial \bar{q}_r$, $\partial \hat{G}_r / \partial \bar{q}_r$ and $\partial \bar{S} / \partial \bar{q}_r$, respectively; $\delta_{\xi'}$, $\delta_{\eta'}$ and $\delta_{\zeta'}$ the three-point central difference operators; $D_{m\xi'}$, $D_{m\eta'}$ and $D_{m\zeta'}$, the implicit dissipation operators; and $D_{e\xi'}$, $D_{e\eta'}$ and $D_{e\zeta'}$ the explicit dissipation operators. The expressions of the dissipation operators are given in ref. 24. The implicit damping coefficient is ϵ_m and the explicit damping coefficients are ϵ_2 and ϵ_4. The damping coefficients are having the same values in the ξ', η' and ζ' directions.

The solution of Eq. (20) is obtained through three successive sweeps in the η', ζ' and ξ'; respectively. Once $\Delta \bar{q}_r^n$ is obtained, $\bar{q}_r^{n+1}$ is found from

$$q_r^{n+1} = \bar{q}_r^n + \Delta \bar{q}_r^n \tag{22}$$

The surface boundary conditions is explicitly enforced through the normal momentum equation[24] while the farfield boundary conditions for subsonic flows are enforced using the inflow-outflow conditions which are based on the Rieman invariants[24].

Computational Results

A sharp-edged delta wing of aspect ratio, AR, of one, at a mean angle of attack, α_m, of 20.5° and in a free stream Mach number, M_∞, of 0.3 is considered for the computational application of the implicit three-dimensional vectorized program. The body conformed grid consists of 80x38x48 cells in the ξ', η' and ζ' directions, respectively; and its size is one root-chord ahead of the wing vertex, two root-chords behind the trailing edge and one root-chord radius in the cross flow planes. The outer boundary consists of a hemi-spherical surface with its center at the wing vertex and a cylindrical surface with its axis coinciding with the wing axis. The grid is generated in cross-flow planes using a modified Joukowski transformation which is locally applied at the grid chord stations with exponential clustering at the wing surface.

Steady Flow:

The implicit program is used to solve for the steady flow at 20.5° angle of attack with two levels of numerical dissipation; a low dissipation (LD) with $\epsilon_2 = 0.05$, $\epsilon_4 = 00.0025$ and

ε_m = 0.25 and a high dissipation (HD) with ε_2 = 0.25, ε_4 = 0.0025 and ε_m = 0.25. Figure 1 shows the solutions at two chord stations of 0.52 and 0.81 on the wing. The figures from left to right show the surface pressure coefficient (Figures 1.1), the static pressure coefficient contours (Figures 1.2) and the cross-flow velocity directions (Figures 1.3). Here, we compare the surface pressure of the Implicit-Scheme with low dissipation with that of the experimental data of Hummel[22]. Other comparisons are given by the authors in ref. 24.

At X'/C = 0.52, the computed surface pressure with low dissipation is in excellent agreement with the experimental data. The computed static pressure contours with low dissipation show higher pressue levels than those computed contours with high dissipation, particularly in the vortical core region. With low dissipation, the highest pressure contour is 1.6, while with high dissipation the highest pressure contour (at the same locatin) is 1.1. Comparison of the computed surface pressure with high dissipation with that of the experimental data (given in ref. 24) shows that the computed peak suction pressure is underpredicted by 13% although the remainder of the surface pressure is in good agreement with the experimental data.

At X'/C = 0.81, the computed surface pressure with low dissipation is higher than that of the experimental data, particularly under the primary vortex core. The computed peak suction pressure is about 25% higher than that of the experimental data. Comparison of the computed static pressure contours with low dissipation shows higher pressure levels than those computed contours with high dissipation, particularly in the vortical core region. The cross flow velocities of both dissipation levels (Figures 1.3) show almost identical shapes and directions.

Figure 2 shows the experimental static pressure contours of Hummel[22] in planes perpendicular to the wind direction (Figures 2.1), the computed static pressure contours in planes perpendicular to the wing surface (Figures 2.2) and the cross-flow velocity directions (Figures 2.3). The computational results along with the experimental data are shown for two cross flow planes in the wake; X'/C = 1.02 and X'/C = 1.25. At X'/C = 1.02, the computed outer contours are in excellent agreement with the experimental contours. For the most inner static pressure contours, the experimental data show higher level than those of the computed results. On the other hand, the implicit results with low dissipation show higher level than those of the higher dissipation. Similar results are seen at X'/C = 1.25. At this location, it is seen that the trailing-edge vortex core is captured using the low-dissipation implicit scheme.

The discrepancies between the experimental data and the computed results with low dissipation level are attributed to the grid coarseness in the vortical core and to the viscous effects in the vortex core as well as on the wing upper surface. The discrepancies between the computed results with low and high dissipation are obviously due to the low and high values of the explicit second-order damping coefficient.

On the VPS-32 computer of NASA Langley Research Center, a typical steady flow case takes 1050 psuedo time stepping to reach a residual error of 10^{-3}.

Unsteady Flow (Pitching Oscillation about the Quarter-Chord Axis):

The steady results with low dissipation level are used as the initial conditions for calculating the unsteady flow around the same wing which is undergoing a pitching oscillation about the quarter chord axis. The angle of attack $\alpha(t)$ is given by

$$\alpha(t) = \alpha_m + \alpha_o \sin 2\sqrt{\gamma}\, M_\infty\, kt$$

where α_o is the amplitude, and k is the reduced frequency ($k = \frac{k^* C}{2U_\infty}$, k^* ≡ dimensional frequency and c ≡ wing chord length). In this application α_m = 20.5°, α_o = 2°, M_∞ = 0.3 and k = 3 which corresponds to a period of 2.95 per cycle. Each cycle of oscillation takes about 1,475 time steps and the solution covers 5,000 time steps which correspond to 3.39 cycles of oscillation. Figure 3 shows α vz t motion at the top, which is followed by the surface pressure variation, static pressure contours and cross-flow velocity in each row of figures. The numbers 1-15 on the α-t curve and on the other figures show the instants at which the computational results are shown. Here, we show the computations at X'/C = 0.52 and the computed surface pressures are shown every 200 time steps starting from the 2,200 time step, which corresponds to point 1 on the α-t curve. The static pressure contours and the cross-flow velocity directions are given at the 3,000; 4,000 and 5,000 time steps which correspond to points 5, 10 and 15, respectively; on the α-t curve. Comparison of the surface pressure at points 7 and 14, corresponding to 2.31 and 3.25, cycles respectively, shows that periodic oscillation has already been reached. Experimental data for unsteady vortex dominated wing flows are urgently needed for bench-mark comparisons.

Concluding Remarks

The three-dimensional unsteady Euler equations in a moving frame of reference are solved by using an implicit approximately-factored finite-volume scheme. The computational applications cover steady low-subsonic flow around a sharp-edged delta wing at a large angle of attack, and unsteady low-subsonic flow around the same wing undergoing a pitching oscillation about the same large angle of attack. The steady flow problem has been computed with two levels of numerical dissipation, and the results have been compared with each other and with the experimental data. The low-dissipation results give better agreement with the experimental data than those of high-dissipation results. However, fine grid embedding are needed in the vortical regions. Moreover, the viscous terms must be added in the vortical regions (free-shear layers)

and in the surface boundary-layer flow. Outside of these regions, Euler equations are adequate for computing the flow field. This calls for urgent extension of the Euler/Navier-Stokes zonal scheme[16] to this problem. The results of the unsteady flow application show consistency, and they show periodic solution in the third cycle of oscillation. Although the code has been verified previously with unsteady airfoil computation[17], unsteady experimental data for vortex dominated flows are urgently needed for bench-mark comparison. Work is underway to use the flux-difference splitting scheme with the unsteady Euler/Navier-Stokes zonal scheme.

Acknowledgement

This research work is supported by NASA Langley Research Center under Grants No. NAG-1-846 and NAG-1-648.

References

1. Whitlow, W., Jr., "Computational Unsteady Aerodynamics for Aeroelastic Analysis, NASA TM 100523, December 1987.

2. Ballhaus, W. F. and Goorjian, P. M., "Implicit Finite-Difference Computations of Unsteady Transonic Flows about Airfoils," AIAA Journal, Vol. 15, No. 12, December 1977, pp. 1728-1735.

3. Edwards, J. W., Bland, S. R. and Seidel, D. A., "Experience with Transonic Unsteady Aerodynamic Calculations," NASA TM-86278, 1984.

4. Batina, J. T., "Unsteady Transonic Algorithm Improvements for Realistic Aircraft Applications," AIAA 88-0105, January 1988.

5. Chipman, R. and Jameson, A., "Full Conservative Numerical Solutions for Unsteady Irrotational Transonic Flow about Airfoils," AIAA 79-1555, July 1979.

6. Goorjian, P. M., "Implicit Computations of Unsteady Transonic Flow Governed by the Full Potential Equation in Conservation Form," AIAA 80-0150, January 1980.

7. Ruo, S. Y., Malon, J. B. and Sankar, L. N., "Steady and Unsteadcy Full Potential Calculation for High and Low Aspect Ratio Supercritical Wings," AIAA 86-0122, January 1986.

8. Batina, J. T., "Unsteady Transonic Small-Disturbance Theory Including Entropy and Vorticity Effects," AIAA 88-2278-CP, April 1988.

9. Whitlow, W., Jr., "Application of a Nonisentropic Full Potential Method to AGARD Standard Airfoils," AIAA 88-0710, January 1988.

10. Howlett, J. T. and Bland, S. R., "Calculation of Viscous Effects on Transonic Flow for Oscillation Airfoils and Comparisons with Experiment," NASA TP-2731, September 1987.

11. Weinberg, B. C. and Shamroth, S. J., "Three-Dimensional Unsteady Viscous Flow Analysis Over Airfoil Sections," NASA CR 172368, 1984.

12. Kandil, O. A. and Chuang, H. A., "Influence of Numerical Dissipation on Computational Euler Equations for Vortex-Dominated Flows," AIAA Journal, Vol. 25, No. 11, November 1987, pp. 1426-1434.

13. Kandil, O. A. and Chuang, H. A., "Computation of Steady and Unsteady Vortex-Dominated Flows," AIAA 87-1462, June 1987. To appear in the AIAA Journal, 1988.

14. Kandil, O. A. and Chuang, H. A., "Unsteady Vortex-Dominated Flows Around Maneuvering Wings Over a Wide Range of Mach Numbers," AIAA 88-0317, January 1988.

15. Holst, T. L., Gundy, K. L., Flores, J., Chaderjian, N. M., Kaynak, U. and Thomas, S. D., "Numerical Solution of Transonic Wing Flows Using an Eule/Navier-Stokes Zonal Approach," AIAA 85-1640, July 1985.

16. Kandil, O. A., Wong, T-C. and Liu, C. H., "Euler/Navier-Stokes Zonal Scheme with Applications to Separated and Isolated-Vortex Flows," AIAA 88-0507, January 1988.

17. Kandil, O. A. and Chuang, H. A., "Unsteady Transonic Airfoil Computation Using Implicit Euler Scheme on Body-Fixed Grid," SECTAM XIV Developments in Theoretical and Applied Mechanics, April 1988, pp. 37-46. Accepted for publication AIAA Journal.

18. Anderson, W. K., Thomas, J. L. and Rumsey, C. L., "Extension and Applications of Flux-Vector Splitting to Unsteady Calculations on Dynamic Meshes," AIAA 87-1152-CP, 1987.

19. Visbal, M. R. and Shang, J. S., "Numerical Investigation of the Flow Structure Around a Rapidly Pitching Airfoils," AIAA 87-1424, June 1987.

20. Rumsey, C. L. and Anderson, W. K., "Some Numerical and Physical Aspects of Unsteady Navier-Stokes Computations Over Airfoils Using Dynamic Meshes," AIAA 88-0329, January 1988.

21. Landon, R., "NACA 0012 Oscillatory and Transient Pitching," Compendium of Unsteady Aerodynamic Measuremnts, AGARD-R-702, 1982.

22. Hummel, O., "On the Vortex Formation Over a Slender Wing at Large Angles of Incidence," AGARD CP-247, January 1979, pp. 15.1-15.17.

23. Kandil, O. A. Chuang, H. A. and Shifflette, J. M., "Finite-Volume Euler and Navier-Stokes Solvers for Three-Dimensional and Conical Vortex Flows Over Delta Wings," AIAA 87-0041, January 1987.

24. Kandil, O. A. and Chuang, H. A., "Prediction of Unsteady Loads on Manuevering Delta Wings Using Time-Accurate Euler Schemes," AIAA-88-2280-CP, April 1988.

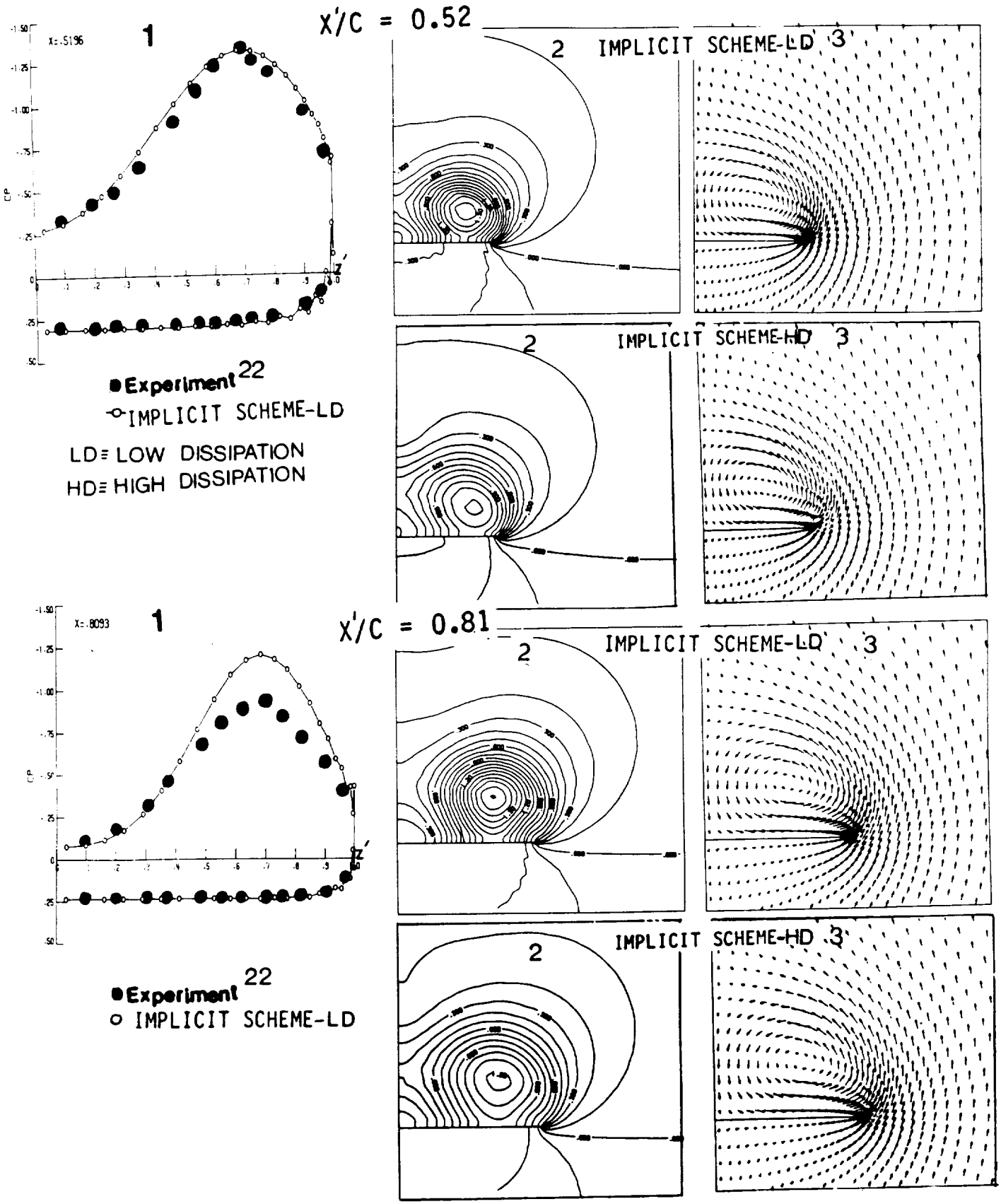

Figure1 . Comparison of the surface pressure,static pressure and cross-flow velocity at two chord stations on the wing for a sharp-edge delta wing, 80x38x48 cell, M_∞ = 0.3, α = 20.50^0, AR = 1; 1. Surface pressure, 2. Static pressure contours, 3. Cross-flow velocity.

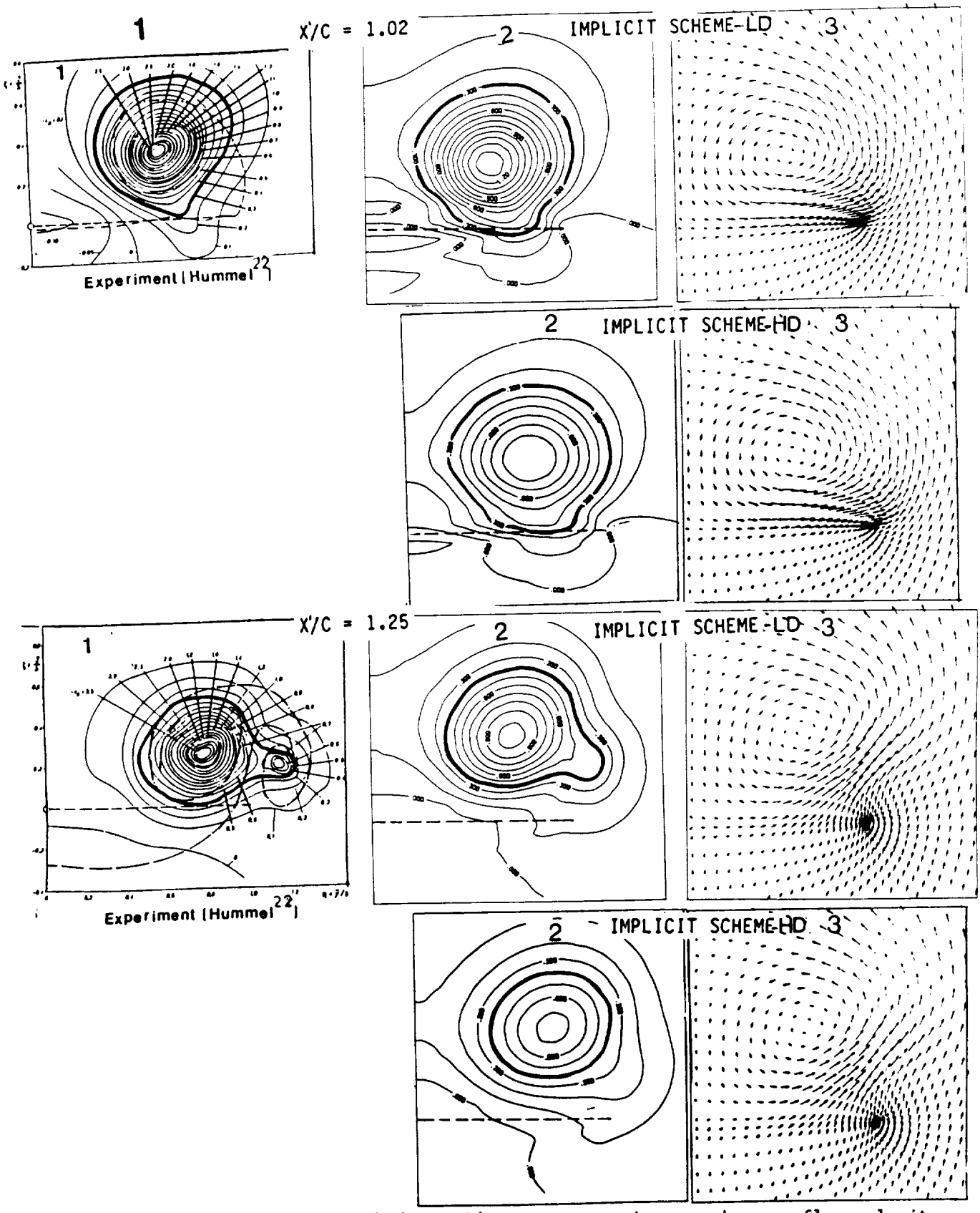

Figure 2. Comparison of the static pressure contours and cross-flow velocity at two chord stations in the wake of a sharp-edge delta wing, 80x38x48 cell, $M_\infty = 0.3$, $\alpha = 20.5^0$, Ar = 1; 1. Experimental static pressure contours, 2. Computed static pressure contours, 3. Cross-flow velocity.

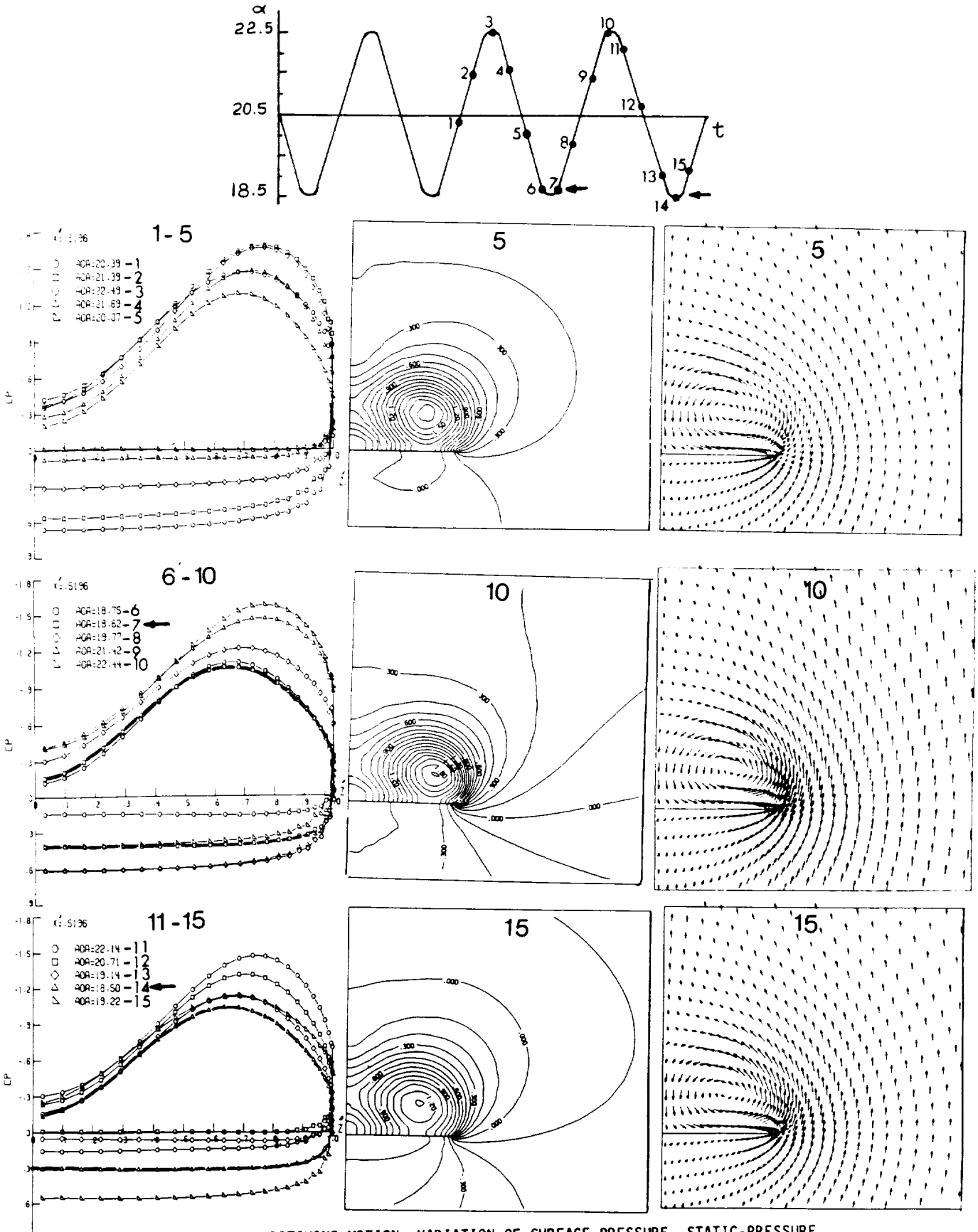

FIGURE 3. PITCHING MOTION, VARIATION OF SURFACE PRESSURE, STATIC-PRESSURE CONTOURS AND CROSS-FLOW VELOCITIES FOR A SHARP-EDGED DELTA WING UNDERGOING PITCHING OSCILLATION; 80X38X48 CELL, $M_\infty = 0.3$, $\alpha_m = 20.5^0$, $\alpha_o = 20^0$, $k = 3$, $AR = 1$, $\epsilon_2 = 0.05$, $\epsilon_4 = 0.0025$, $\epsilon_m = 0.25$.

To Appear in
AIAA Journal, September

COMPUTATION OF VORTEX-DOMINATED FLOW FOR A DELTA WING UNDERGOING PITCHING OSCILLATION†

Osama A. Kandil* and H. Andrew Chuang**
Old Dominion University, Norfolk, Virginia

Abstract

The conservative unsteady Euler equations for the flow relative to a moving frame of reference are used to solve for the three-dimensional steady and unsteady flows around a sharp-edged delta wing. The resulting equations are solved by using an implicit, approximately-factored, finite-volume scheme. Implicit second-order and explicit second- and fourth-order dissipations are added to the scheme. The boundary conditions are explicitly satisfied. The grid is generated by locally using a modified Joukowski transformation in cross-flow planes at the grid chord stations. The computational applications cover a steady flow around a delta wing whose results serve as the initial conditions for the unsteady flow around a pitching delta wing at a large mean angle of attack. The steady results are compared with the experimental data and the unsteady results are compared with results of a flux-difference splitting scheme.

---

†This paper has been presented as AIAA-88-3649-CP, Cincinnati, Ohio, 1988.

*Professor, Department of Mechanical Engineering and Mechanics, Associate Fellow AIAA.

**Visiting Assistant Professor, Same Department, Member AIAA.

Introduction

Unsteady flows around delta wings are characterized by the existence of unsteady large- and small-scale vortices (primary, secondary and possible tertiary vortices), moving shock waves with time-dependent strengths, time-dependent vortex-core formation and breakdown (bubble and spiral types of vortex breakdown), and interaction of shock waves with the vortical-region and the surface-boundary-layer flows. These highly unsteady aerodynamic loads may interact with the wing structural response causing aeroelastic instabilities which may restrict the aircraft flight envelope. In Ref. 1, the status of computational unsteady aerodynamics for aeroelastic analysis has been discussed, and recommendations for future code development for separated and vortex-dominated flows are presented.

The literature on the computational solution and experimental data of the unsteady vortex-dominated flows, particularly in the transonic regime, is unfortunately very limited. This is attributed to the complexity of the flow and its dependence on numerous parameters, and the substantial computational cost involved for the flow resolution and the time-accurate computations.

Most of the existing unsteady computational schemes for airfoil and wing flow applications are based on the unsteady small disturbance (UTSD) theory[2-4], unsteady full potential (UFP) equation[5-7], UTSD theory with vorticity and non-isentropic flow corrections[8] and UFP equation with non-isentropic flow corrections[9]. These schemes are restricted to attached flows only, and hence they cannot be used to capture vortex-dominated flows. For mildly separated flows, integral and finite-difference boundary-layer schemes have been coupled with potential flow schemes[10,11]. However, such schemes cannot be used for massive separation.

On the other hand, the unsteady Euler equations adequately model shock waves and their motion, entropy increase across shocks and entropy gradient and vorticity production and convection behind shocks, as can be seen from Crocco's theorem and the inviscid vorticity transport equation. Moreover, the computational solution of Euler equations adequately models separated flows from sharp edges[12-14]. For smooth-surface separation, round-edge separation, shock-induced separation, viscous diffusion and dissipation, vortex breakdown, flow transition and turbulence; viscous terms must be added to Euler equations to recover the full Navier-Stokes equations or an approximate form of these equations. Although the process of adding the viscous terms to the unsteady Euler solvers is simple and straightforward, the computational cost for high-Reynolds-number unsteady flows is substantial and might be prohibitive due to the need for using fine grids to adequately resolve the viscous effects.

Euler/Navier-Stokes zonal approaches[15,16] have been demonstrated to maintain the accuracy of the Navier-Stokes solutions and in the meantime, alleviate to a good extent the computational cost of the Navier-Stokes equations. These approaches along with fine grid embedding in the vortical regions should be developed further for unsteady flows.

Recently, successful time accurate solutions of the unsteady Euler and Navier-Stokes equations have been presented for airfoils[14,17-20]. The only existing unsteady Euler solutions for vortex-dominated flows are those for the rolling-oscillation of a sharp-edge delta wing in a locally conical supersonic flow around a mean angle of attack and a zero angle of attack, which were presented by the authors in Refs. 13 and 14. The authors derived the unsteady Euler equations for the flow relative to a moving frame of reference, and the equations have been solved by using an explicit, multi-stage Runge-Kutta time stepping, finite-volume scheme. By casting the equations in a moving frame of

reference, we eliminated the computation of the grid motion. Moreover, since the equations are expressed in terms of the flow vector field relative to the moving frame, the equations still preserve the conservation form. Periodic solutions were achieved in the third cycle of rolling oscillation. Details of the surface pressure, cross-flow velocity and cross-flow Mach contours were presented showing the primary- vortex and shock-wave formation, interaction and disappearance.

In the present paper, the three-dimensional unsteady Euler equations in a moving frame of reference are solved by using an implicit approximately-factored, finite-volume scheme. The resulting code has been validated through the solution of unsteady flows around airfoils undergoing pitching oscillation[17], and comparison of the computed results with the experimental data of ref. 21. The present three-dimensional steady results are compared with the experimental data of ref. 22 for two levels of explicit dissipation. With the steady results serving as initial conditions for the unsteady flow, the flow around the same delta wing undergoing pitching oscillation about the quarter-chord axis is solved in this paper. The results of the pitching delta wing are compared with those obtained using the three-dimensional flux-difference splitting scheme of ref. 20.

Formulation

Starting with the conservative form of the unsteady Euler equations for the flow relative to a space-fixed frame of reference, and using the following relations for the substantial and local derivatives of a scalar "a" and a vector "$\bar{A}$"

$$\frac{Da}{Dt} = \frac{D'a}{Dt'} \tag{1.a}$$

$$\frac{\partial a}{\partial t} = \frac{\partial' a}{\partial t'} - \bar{V}_t \cdot \nabla a \tag{1.b}$$

$$\frac{D\bar{A}}{Dt} = \frac{D'\bar{A}}{Dt'} + \bar{\omega}\times\bar{A} \tag{1.c}$$

$$\frac{\partial \bar{A}}{\partial t} = \frac{\partial' \bar{A}}{\partial t'} - \bar{V}_t \cdot \nabla\bar{A} + \bar{\omega}\times\bar{A} \tag{1.d}$$

we obtain the conservative unsteady Euler equations for the flow relative to a moving-frame of reference. In terms of the Cartesian coordinates x', y', z' of the moving-frame of reference, the resulting Euler equations are

$$\frac{\partial' \bar{q}_r}{\partial t'} + \frac{\partial' \bar{E}_r}{\partial x'} + \frac{\partial' \bar{F}_r}{\partial y'} + \frac{\partial' \bar{G}_r}{\partial z'} = \bar{S} \tag{2}$$

where

$$\bar{q}_r = [\rho,\ \rho u_r,\ \rho v_r,\ \rho w_r,\ \rho e_r]^t \tag{3}$$

$$\bar{E}_r = [\rho u_r,\ \rho u_r^2 + p,\ \rho u_r v_r,\ \rho u_r w_r,\ \rho u_r h_r]^t \tag{4}$$

$$\bar{F}_r = [\rho v_r,\ \rho u_r v_r,\ \rho v_r^2 + p,\ \rho v_r w_r,\ \rho v_r h_r]^t \tag{5}$$

$$\bar{G}_r = [\rho w_r,\ \rho u_r w_r,\ \rho v_r w_r,\ \rho w_r^2 + p,\ \rho w_r h_r]^t \tag{6}$$

$$\begin{aligned}\bar{S} = [0,\ &-\rho a_{tx'},\ -\rho a_{ty'},\ -\rho a_{tz'},\\ &-\rho[\bar{V}_r \cdot \bar{a}_o + (\bar{\omega}\times\bar{r}) \cdot \bar{a}_o + \bar{V}_o \cdot (\bar{a}_t - \bar{\omega}\times\bar{V}_r)\\ &+ \bar{V}_r \cdot \dot{(\bar{\omega}\times\bar{r})} + (\bar{\omega}\times\bar{r}) \cdot \dot{(\bar{\omega}\times\bar{r})}]]^t\end{aligned} \tag{7}$$

$$\begin{aligned}e_r &= e - \bar{V} \cdot \bar{V}_t\\ &= \frac{p}{\rho(\gamma-1)} + \frac{V_r^2}{2} - \frac{V_t^2}{2}\end{aligned} \tag{8}$$

$$h_r = h - \bar{V} \cdot \bar{V}_t$$
$$= \frac{\gamma p}{\rho(\gamma-1)} + \frac{V_r^2}{2} - \frac{V_t^2}{2} \tag{9}$$

$$\bar{V}_t = \bar{V} - \bar{V}_r = \bar{V}_o + \bar{\omega} \times \bar{r} \tag{10}$$

$$\bar{a}_t = \bar{a} - \bar{a}_r$$
$$= \frac{D\bar{V}}{Dt} - \frac{D'\bar{V}_r}{Dt'}$$
$$= \bar{a}_o + \dot{\bar{\omega}} \times \bar{r} + 2\bar{\omega} \times \bar{V}_r + \bar{\omega} \times (\bar{\omega} \times \bar{r}) \tag{11}$$

$$\bar{\omega} = \omega_x \hat{i} + \omega_y \hat{j} + \omega_z \hat{k}$$
$$= (-\dot{\alpha} \sin\beta + \dot{\theta})\,\hat{i}$$
$$+ (\dot{\alpha} \cos\beta \sin\theta + \dot{\beta} \cos\theta)\,\hat{j}$$
$$+ (\dot{\alpha} \cos\beta \cos\theta - \dot{\beta} \sin\theta)\,\hat{k} \tag{12}$$

In Eqs. (1)-(12), $\bar{q}_r$ is the flow vector field of relative motion; $\bar{E}_r$, $\bar{F}_r$ and $\bar{G}_r$ the inviscid fluxes of the relative motion, $\bar{S}$ a source term due to the motion of the reference frame, ρ the density, p the pressure, e and h the total energy and total enthalpy per unit mass, $\bar{V}$ and $\bar{a}$ the absolute velocity and absolute acceleration of the flow, $\bar{V}_r$ and $\bar{a}_r$ the flow relative velocity and relative acceleration, $\bar{V}_t$ and $\bar{a}_t$ the transformation velocity and transformation acceleration, $\bar{V}_o$ and $\bar{a}_o$ the translation velocity and translation acceleration of the moving frame, $\bar{\omega}$ and $\dot{\bar{\omega}}$ the angular velocity and angular acceleration of the moving frame, $\bar{r}$ the position vector of a fluid particle with respect to the moving frame, and γ is the ratio of specific

heats. The pitch, yaw and roll angles are referred to by using the Eulerian angles α, β and θ; respectivley. The "'" refers to the derivatives, time or coordinates with respect to the moving frame of reference. Equation (2) shows that the present formulation is in a conservation form. However, the conservation form is not a strong one due to the existence of the source term on the right hand side. But on the other hand, the Jacobian corresponding to this term is not spatially differenced (see Eqs. 21 and 22) and hence the truncation error of this term is mainly due to temporal differencing.

Introducing the curvilinear coordinates ξ', η' and ζ' in the moving frame of reference, which are given by

$$\xi' = \xi'(x',y',z'), \quad \eta' = \eta'(x',y',z'),$$

$$\zeta' = \zeta'(x',y',z') \tag{13}$$

Eqs. (2)-(7) are transformed to

$$\frac{\partial'\hat{Q}_r}{\partial t'} + \frac{\partial'\hat{E}_r}{\partial \xi'} + \frac{\partial'\hat{F}_r}{\partial \eta'} + \frac{\partial'\hat{G}_r}{\partial \zeta'} = \hat{S} \tag{14}$$

$$\hat{Q}_r = J^{-1}\,[\rho,\ \rho u_r,\ \rho v_r,\ \rho w_r,\ \rho e_r]^t \tag{15}$$

$$\hat{E}_r = J^{-1}\,[\rho U_r,\ \rho u_r U_r + \xi'_x,\ p,\ \rho v_r U_r + \xi'_y,\ p,$$

$$\rho w_r U_r + \xi'_z,\ p,\ \rho U_r h_r]^t \tag{16}$$

$$\hat{F}_r = J^{-1}[\rho V_r,\ \rho u_r V_r + \eta'_x,\ p,\ \rho v_r V_r + \eta'_y,\ p,$$

$$\rho w_r V_r + \eta'_z,\ p,\ \rho V_r h_r]^t \tag{17}$$

$$\hat{G}_r = J^{-1}[\rho W_r,\ \rho u_r W_r + \zeta'_x,\ p,\ \rho v_r W_r + \zeta'_y,\ p,$$

$$\rho w_r W_r + \zeta'_z,\ p,\ \rho W_r h_r]^t \tag{18}$$

$$\hat{S} = J^{-1}\bar{S} \tag{19}$$

In Eqs. (15)-(19), J^{-1} is the Jacobian of transformation and U_r, V_r and W_r are the contravariant velocity components.

Computational Scheme

Equation (14) is integrated over ξ', η' and ζ' and the divergence theorem is applied to the resulting equation. By using the implicit approximate factorization scheme, we obtain the following difference equation for a typical cell (i, j, k)

$$\left[\frac{I}{J\Delta t'} + \delta_{\xi'}A^n_r - \frac{H^n_r}{J} - D_{m\xi'}\right] x$$

$$\left[\frac{I}{J\Delta t'} + \delta_{\eta'}B^n_r - D_{m\eta'}\right] x$$

$$\left[\frac{I}{J\Delta t'} + \delta_{\zeta'}C^n_r - D_{m\zeta'}\right] \Delta q^n_r = -\frac{1}{(J\Delta t')^2}\bar{W}(\bar{q}^n_r) \tag{20}$$

where

$$\begin{aligned}\bar{W}(\bar{q}^n_r) = {} & (\hat{E}^n_{r\,i+1/2,j,k} - \hat{E}^n_{r\,i-1/2,j,k}) \\ & + (\hat{F}^n_{r\,i,j+1/2,k} - \hat{F}^n_{r\,i,j-1/2,k}) \\ & + (\hat{G}^n_{r\,i,j,k+1/2} - \hat{G}^n_{r\,i,j,k-1/2}) \\ & - \hat{S}^n_{i,j,k} - D_{e\xi'}(\bar{q}^n_r) \\ & - D_{e\eta'}(\bar{q}^n_r) - D_{e\zeta'}(\bar{q}^n_r)\end{aligned} \tag{21}$$

In Eqs. (20) and (21), A_r, B_r, C_r and H_r are the Jacobian matrices $\partial\hat{E}_r/\partial\bar{q}_r$, $\partial\hat{F}_r/\partial\bar{q}_r$, $\partial\hat{G}_r/\partial\bar{q}_r$ and $\partial\bar{S}/\partial\bar{q}_r$, respectively; $\delta_{\xi'}$, $\delta_{\eta'}$ and $\delta_{\zeta'}$ the three-point central difference operators; $D_{m\xi'}$, $D_{m\eta'}$ and $D_{m\zeta'}$ the implicit dissipation operators; and $D_{e\xi'}$, $D_{e\eta'}$ and $D_{e\zeta'}$ the explicit dissipation operators. The expressions of the dissipation operators in the ξ' direction are given by

$$D_{m\xi'} = \varepsilon_m I \left(\frac{CFL}{J\Delta t^*}\right) (\Delta\nabla)_{\xi'} \tag{22}$$

$$D_{e\xi'} = \nabla_{\xi'} \left(\frac{J^{-1}_{i+1,j,k}}{\Delta t^*_{i+1,j,k}} + \frac{J^{-1}_{i,j,k}}{\Delta t^*_{i,j,k}}\right) \left(\nu^{(2)}_{i,j,k}\, \Delta_{\xi'} - \nu^{(4)}_{i,j,k}\, \Delta_{\xi'}\, \nabla_{\xi'}\, \Delta_{\xi'}\right) \tag{23}$$

$$\nu^{(2)}_{i,j,k} = \varepsilon_2 \max\left(\lambda_{i+1,j,k},\ \lambda_{i,j,k}\right) \tag{24}$$

$$\nu^{(4)}_{i,j,k} = \max\left(0,\ \varepsilon_4\, \Delta t^* - \nu^{(2)}_{i,j,k}\right) \tag{25}$$

$$\lambda_{i,j,k} = \frac{\left|p^n_{i+1,j,k} - 2\, p^n_{i,j,k} + p^n_{i-1,j,k}\right|}{\left|p^n_{i+1,j,k} + 2\, p^n_{i,j,k} + p^n_{i-1,j,k}\right|} \tag{26}$$

$$\Delta t^* = \frac{\Delta t'}{CFL} = \frac{1}{|U_r| + |V_r| + |W_r| + a\left(|\nabla\xi'| + |\nabla\eta'| + |\nabla\zeta'|\right)} \tag{27}$$

where U_r, V_r and W_r are the contravariant components of the relative velocity. The implicit damping coefficient is ε_m and the explicit damping coefficients are ε_2 and ε_4. The damping coefficients are having the same values in the ξ', η' and ζ' directions.

The solution of Eq. (20) is obtained through three successive sweeps in the η', ζ' and ξ'; respectively. Once $\Delta\bar{q}^n_r$ is obtained, $\bar{q}^{n+1}_r$ is found from

$$q^{n+1}_r = \bar{q}^n_r + \Delta\bar{q}^n_r \tag{28}$$

Boundary Conditions

The surface boundary condition is enforced explicitly through the normal momentum equation

$$\frac{\partial P}{\partial n} = \rho \bar{V}_r \cdot (\bar{V}_r \cdot \nabla \hat{n}) - \rho \hat{n} \cdot \bar{a}_t \tag{29}$$

where $\hat{n}$ is the unit normal of the wing surface. Also, the farfield boundary conditions are enforced explicitly. In the present application, subsonic flow in the farfield is considered and hence, the inflow-outflow boundary conditions are based on the Riemann invariants, R_∞ and R_i, for one-dimensional flow normal to the boundary which are given by

$$R_\infty = \bar{V}_\infty \cdot \hat{n} - \frac{2}{\gamma-1} (\gamma p_\infty/\rho_\infty)^{1/2} \tag{30}$$

$$R_i = \bar{V}_i \cdot \hat{n} + \frac{2}{\gamma-1} (\gamma p_i/\rho_i)^{1/2} \tag{31}$$

where $\hat{n}$ is the unit normal of the outer boundary of the computational region and the subscripts ∞ and i refer to the farfield conditions and the values extrapolated from the interior cells at the boundary, respectively. Thus, the inflow boundary conditions are given by

$$(\bar{V} \cdot \hat{n})_b = \frac{1}{2} (R_\infty + R_i) \tag{32.a}$$

$$(p/\rho)_b = \frac{1}{\gamma} \left[\frac{\gamma-1}{4} (R_i - R_\infty)\right]^2 \tag{32.b}$$

$$(p/\rho^\gamma)_b = (P/\rho^\gamma)_\infty \tag{32.c}$$

$$(\bar{V} \cdot \hat{t})_b = (\bar{V} \cdot \hat{t})_\infty \tag{32.d}$$

where b refers to the boundary and $\hat{t}$ is a unit vector tangential to the boundary. For the out-flow boundary conditions, the subscript ∞ in Eqs. (32.c) and (32.d) is replaced by the subscript i. Equations (32.a) and (32.b)

give a complete definition of the flow at subsonic boundaries. Symmetric flow conditions are used at the plane of symmetry for the present application.

Computational Results

A sharp-edged delta wing of aspect ratio, AR, of one, at a mean angle of attack, α_m, of 20.5° and in a free stream Mach number, M_∞, of 0.3 is considered for the computational application of the implicit three-dimensional vectorized program. The body conformed grid consists of 80x38x48 cells in the ξ', η' and ζ' directions, respectively; and its size is one root-chord ahead of the wing vertex, two root-chords behind the trailing edge and one root-chord radius in the cross flow planes. The size of the computational domain has been determined through numerical experiments, where the maximum absolute value of the difference of the pressure coefficient did not exceed 0.5% from that of a computational domain which has double the present computational size. The small computational domain is used because of the limited available computational resources. The outer boundary consists of a hemi-spherical surface with its center at the wing vertex and a cylindrical surface with its axis coinciding with the wing axis. The grid is generated in cross-flow planes using a modified Joukowski transformation which is locally applied at the grid chord stations with exponential clustering at the wing surface.

Steady Flow:

The implicit program is used to solve for the steady flow at 20.5° angle of attack with two levels of numerical dissipation; a low dissipation (LD) with $\varepsilon_2 = 0.05$, $\varepsilon_4 = 00.0025$ and $\varepsilon_m = 0.25$ and a high dissipation (HD) with $\varepsilon_2 = 0.25$, $\varepsilon_4 = 0.0025$ and $\varepsilon_m = 0.25$. As a general principle, the dissipation level in a computational scheme must be as low as possible. But

it must be enough to obtain a stable solution. Although we are dealing with a low subsonic low, where shocks do not exist, second-order dissipation terms are required due to the large gradients in the vortical region. The purpose of this numerical experiment is to determine a low dissipation level, which gives a stable solution also. Figures 1 and 2 show the solutions at two chord stations of 0.52 and 0.81 on the wing, respectively. The figures from left to right show the surface pressure coefficient (Figures 1.1 and 2.1), the static pressure coefficient contours (Figures 1.2 and 2.2) and the cross-flow velocity directions (Figures 1.3 and 2.3). Here, we compare the surface pressure of the Implicit-Scheme with low dissipation with that of the experimental data of Hummel[22]. Other comparisons are given by the authors in ref. 24.

In Figure 1, the computed surface pressure with low dissipation is in excellent agreement with the experimental data. The computed static pressure contours with low dissipation show higher pressure levels than those computed contours with high dissipation, particularly in the vortical core region. With low dissipation, the highest pressure contour is 1.6, while with high dissipation the highest pressure contour (at the same location) is 1.1. The cross-flow velocities of both dissipation levels show almost identical shapes and directions. Comparison of the computed surface pressure with high dissipation with that of the experimental data (given in ref. 24) shows that the computed peak suction pressure is underpredicted by 18% although the remainder of the surface pressure is in good agreement with the experimental data.

In Figure 2, the computed surface pressure with low dissipation is higher than that of the experimental data, particularly under the primary vortex core. It should be noted here that the experimental data of Hummel shown in

Fig. 2.1 is the average of his data at X'/C = 0.7 and 0.9 in ref. 22. The computed peak suction pressure is about 25% higher than that of the experimental data. Comparison of the computed static pressure contours with low dissipation shows higher pressure levels than those computed contours with high dissipation, particularly in the vortical core region. With low dissipation, the highest pressure contour is 1.7, while with high dissipation the highest pressure contour is 1.2. The cross flow velocities of both dissipation levels show almost identical shapes and directions.

Figures 3 and 4 shows the experimental static pressure-coefficient contours of Hummel[22] in planes perpendicular to the wind direction (Figures 3.1 and 4.1), the computed static pressure-coefficient contours in planes perpendicular to the wing surface (Figures 3.2 and 4.2) and the cross-flow velocity directions (Figures 4.3 and 4.4). The computational results along with the experimental data are shown for two cross-flow planes in the wake; X'/C = 1.02 and X'/C = 1.25. In Figure 3, the computed static pressure contours of the outer vortex-core region are in excellent agreement with the experimental contours. For the most inner static pressure contours (levels higher than 0.3), the experimental data show higher level than those of the computed results. On the other hand, the results of static pressure contours of the implicit scheme with low dissipation show higher pressure levels than those with the high dissipation. Similar results are seen at X'/C = 1.25 (Figure 4). At this location, it is seen that the outer contour of the trailing-edge vortex core is captured using the low-dissipation implicit scheme (contour level of 0.4). The cross-flow velocities at X'/C = 1.25 also show that the trailing-edge vortex core has been captured.

The discrepancies between the experimental data and the computed results with low dissipation level are attributed to the grid coarseness in the

vortical core and more important to the viscous effects in the vortex core as well as on the wing upper surface. The discrepancies between the computed results with low and high dissipation are obviously due to the low and high value of the explicit second-order damping coefficient.

On the VPS-32 computer of NASA Langley Research Center, the CPU time is 40 μ sec. per grid point per time step and a typical steady flow case takes 1050 psuedo time stepping to reach a residual error of 10^{-3}.

Unsteady Flow (Pitching Oscillation about the Quarter-Chord Axis):

The steady results with low dissipation level, best level for a stable solution, are used as the initial conditions for calculating the unsteady flow around the same wing which is undergoing a pitching oscillation about the quarter-chord axis. The angle of attack $\alpha(t)$ is given by

$$\alpha(t) = \alpha_m + \alpha_0 \sin 2\sqrt{\gamma}\, M_\infty kt \qquad (33)$$

where α_0 is the amplitude, and k is the reduced frequency ($k = \frac{k^* C}{2U_\infty}$, $k^* \equiv$ dimensional frequency and $c \equiv$ wing chord length). In this application $\alpha_m = 20.5°$, $\alpha_0 = 2°$, $M_\infty = 0.3$ and $k = 3$ which corresponds to a period of 2.95 per cycle. Each cycle of oscillation takes about 1,475 time steps and the solution covers 5,000 time steps which correspond to 3.39 cycles of oscillation.

Figure 5 shows α vz t motion at the top, which is followed by the surface pressure variation, static pressure contours and cross-flow velocity in each row of figures. The numbers 1-15 on the α-t curve and on the other figures indicate the instants at which the computational results are shown. Here, we show the computations at the chord station X'/C = 0.52 and the computed surface pressures are shown every 200 time steps starting from the 2,200 time step, which corresponds to point 1 on the α-t curve. The static

pressure contours and the cross-flow velocity directions are given at the 3,000; 4,000 and 5,000 time steps which correspond to points 5, 10 and 15, respectively; on the α-t curve. Comparison of the surface pressure at points 7 and 14, corresponding to 2.31 and 3.25, cycles respectively, shows that periodic oscillation has already been reached.

Considering the time-history of the surface pressures, which are indicated by the numbers 1-5, 6-10 and 11-15, the variation of the surface pressure and the motion of the primary vortex are predicted as the wing pitching motion (α vz t curve) is progressing. For example, the curves 1-5 show that as the angle of attack increases from instant 1 to instant 2, the peak suction pressure increases and the primary vortex moves outboard in the spanwise direction. This is physically expected since the primary vortex strength increases. As the angle of attack increases from instant 2 to instant 3, the peak suction pressures reaches a maximum value and decreases indicating that the peak suction pressure is leading the wing motion. As the angle of attack decreases from instant 3 to instant 5, the peak suction pressure decreases and the primary vortex moves inboard in the spanwise direction.

On the surface pressure curves, we also show comparisons at selected instants with the computations of Rumsey[25]. Rumsey's computations are produced using a three-dimensional, implicit, flux-difference splitting program, which is known as "CFL3D". The results are computed by using our grid which is used to compute our results. The results are in good agreement and hence the comparison adds confidence to the computational results. Experimental data for the unsteady vortex-dominated wing flows are urgently needed for bench-mark comparisons. However, it is emphasized here that our present scheme and code have been validated earlier[17] for unsteady flows around pitching airfoils using available experimental data.[21]

Concluding Remarks

The three-dimensional unsteady Euler equations in a moving frame of reference are solved by using an implicit approximately-factored finite-volume scheme. The computational applications cover steady low-subsonic flow around a sharp-edged delta wing at a large angle of attack, and unsteady low-subsonic flow around the same wing undergoing a pitching oscillation about the same large angle of attack. The unsteady application presents pioneering results for the first time that we know of. The steady flow problem has been computed with two levels of numerical dissipation, and the results have been compared with each other and with the experimental data. The low-dissipation results give better agreement with the experimental data than those of high-dissipation results. However, fine grid embedding are needed in the vortical regions. Moreover, the viscous terms must be added for accurate computations of the vortex-core regions (free-shear layers) and for the surface boundary-layer flow computations as well. Outside of these regions, Euler equations are adequate for computing the flow field. This calls for urgent extension of the Euler/Navier-Stokes zonal scheme[16] to this problem. The results of the unsteady flow application show consistency, and they show periodic solution in the third cycle of oscillation. The present unsteady results have been compared with those of the flux-difference splitting scheme, and they are in good agreement. Although the code has also been verified previously with unsteady airfoil computation[17], unsteady experimental data for vortex dominated flows are urgently needed for bench-mark comparison.

Acknowledgement

This research work is supported by NASA Langley Research Center under Grants No. NAG-1-846 and NAG-1-648. The authors would like to thank Mr. C. L. Rumsey for computing the pitching delta wing case using the CFL3D code.

References

1. Whitlow, W., Jr., "Computational Unsteady Aerodynamics for Aeroelastic Analysis, NASA TM 100523, December 1987.

2. Ballhaus, W. F. and Goorjian, P. M., "Implicit Finite-Difference Computations of Unsteady Transonic Flows about Airfoils," AIAA Journal, Vol. 15, No. 12, December 1977, pp. 1728-1735.

3. Edwards, J. W., Bland, S. R. and Seidel, D. A., "Experience with Transonic Unsteady Aerodynamic Calculations," NASA TM-86278, 1984.

4. Batina, J. T., "Unsteady Transonic Algorithm Improvements for Realistic Aircraft Applications," AIAA 88-0105, January 1988.

5. Chipman, R. and Jameson, A., "Full Conservative Numerical Solutions for Unsteady Irrotational Transonic Flow about Airfoils," AIAA 79-1555, July 1979.

6. Goorjian, P. M., "Implicit Computations of Unsteady Transonic Flow Governed by the Full Potential Equation in Conservation Form," AIAA 80-0150, January 1980.

7. Ruo, S. Y., Malone, J. B. and Sankar, L. N., "Steady and Unsteadcy Full Potential Calculation for High and Low Aspect Ratio Supercritical Wings," AIAA 86-0122, January 1986.

8. Batina, J. T., "Unsteady Transonic Small-Disturbance Theory Including Entropy and Vorticity Effects," AIAA 88-2278-CP, April 1988.

9. Whitlow, W., Jr., "Application of a Nonisentropic Full Potential Method to AGARD Standard Airfoils," AIAA 88-0710, January 1988.

10. Howlett, J. T. and Bland, S. R., "Calculation of Viscous Effects on Transonic Flow for Oscillating Airfoils and Comparisons with Experiment," NASA TP-2731, September 1987.

11. Weinberg, B. C. and Shamroth, S. J., "Three-Dimensional Unsteady Viscous Flow Analysis Over Airfoil Sections," NASA CR 172368, 1984.

12. Kandil, O. A. and Chuang, H. A., "Influence of Numerical Dissipation on Computational Euler Equations for Vortex-Dominated Flows," AIAA Journal, Vol. 25, No. 11, November 1987, pp. 1426-1434.

13. Kandil, O. A. and Chuang, H. A., "Computation of Steady and Unsteady Vortex-Dominated Flows," AIAA 87-1462, June 1987. Also AIAA Journal, Vol. 26, No. 5, May 1988, pp. 524-531.

14. Kandil, O. A. and Chuang, H. A., "Unsteady Vortex-Dominated Flows Around Maneuvering Wings Over a Wide Range of Mach Numbers," AIAA 88-0317, January 1988.

15. Holst, T. L., Gundy, K. L., Flores, J., Chaderjian, N. M., Kaynak, U. and Thomas, S. D., "Numerical Solution of Transonic Wing Flows Using an Euler/Navier-Stokes Zonal Approach," AIAA 85-1640, July 1985.

16. Liu, C. H., Wong, T. C. and Kandil, O. A., "Separation-Bubble Flow Solution Using Euler/Navier-Stokes Zonal Approach with Downstream Compatibility Conditions," Journal of Scientific Computing, Vol. 3, No. 2, 1988, pp. 121-137.

17. Kandil, O. A. and Chuang, H. A., "Unsteady Transonic Airfoil Computation Using Implicit Euler Scheme on Body-Fixed Grid," AIAA Journal, Vol. 27, No. 8, August 1989, pp. 1031-1037.

18. Anderson, W. K., Thomas, J. L. and Rumsey, C. L., "Extension and Applications of Flux-Vector Splitting to Unsteady Calculations on Dynamic Meshes," AIAA 87-1152-CP, 1987.

19. Visbal, M. R. and Shang, J. S., "Numerical Investigation of the Flow Structure Around a Rapidly Pitching Airfoils," AIAA 87-1424, June 1987.

20. Rumsey, C. L. and Anderson, W. K., "Some Numerical and Physical Aspects of Unsteady Navier-Stokes Computations Over Airfoils Using Dynamic Meshes," AIAA 88-0329, January 1988.

21. Landon, R., "NACA 0012 Oscillatory and Transient Pitching," Compendium of Unsteady Aerodynamic Measuremnts, AGARD-R-702, 1982.

22. Hummel, O., "On the Vortex Formation Over a Slender Wing at Large Angles of Incidence," AGARD CP-247, January 1979, pp. 15.1-15.17.

23. Kandil, O. A. Chuang, H. A. and Shifflette, J. M., "Finite-Volume Euler and Navier-Stokes Solvers for Three-Dimensional and Conical Vortex Flows Over Delta Wings," AIAA 87-0041, January 1987.

24. Kandil, O. A. and Chuang, H. A., "Prediction of Unsteady Loads on Manuevering Delta Wings Using Time-Accurate Euler Schemes," AIAA-88-2280-CP, April 1988, pp. 504-512.

25. Rumsey, C. L., private communications, July 1988.

List of Figures

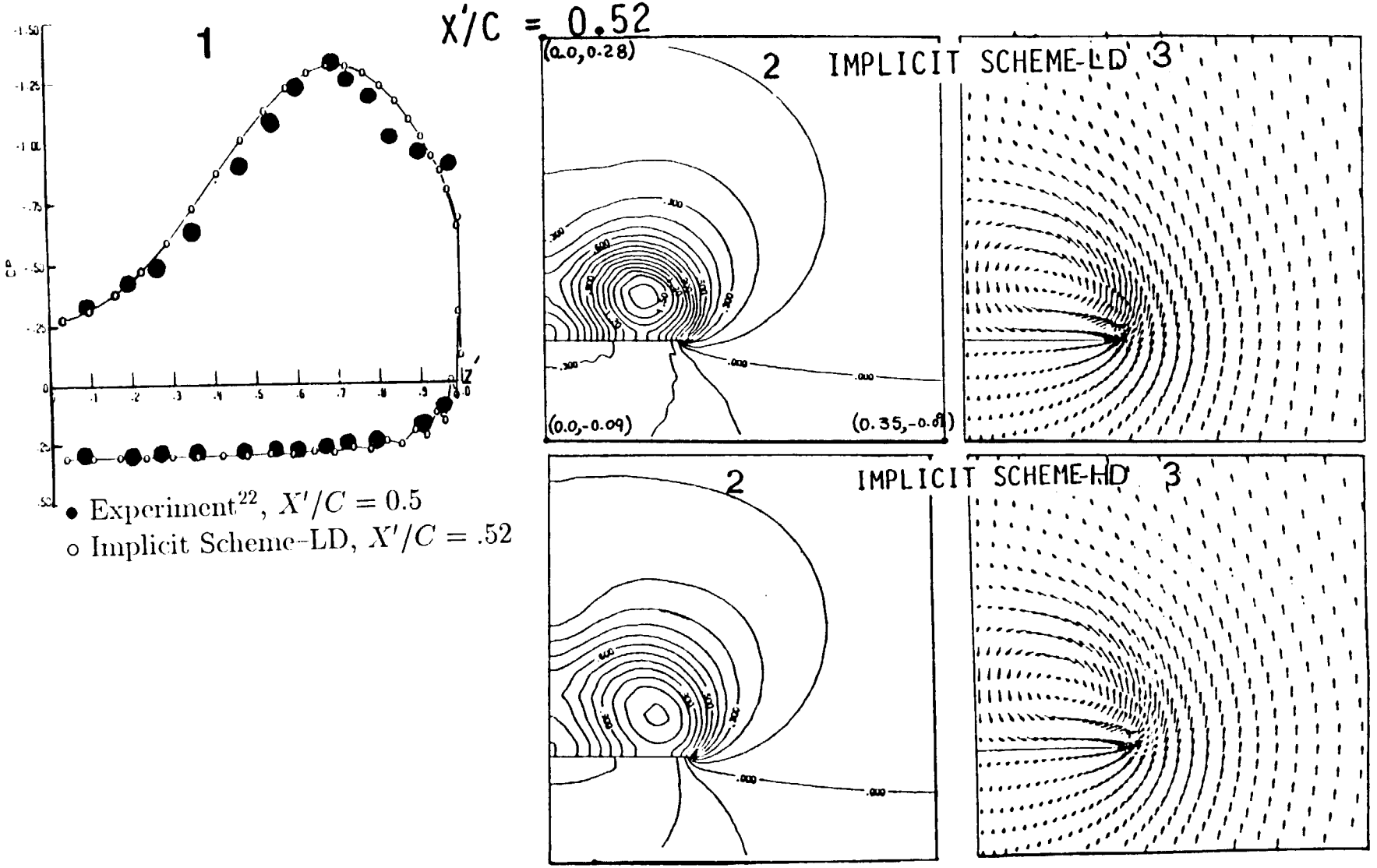

● Experiment[22], $X'/C = 0.5$

○ Implicit Scheme–LD, $X'/C = .52$

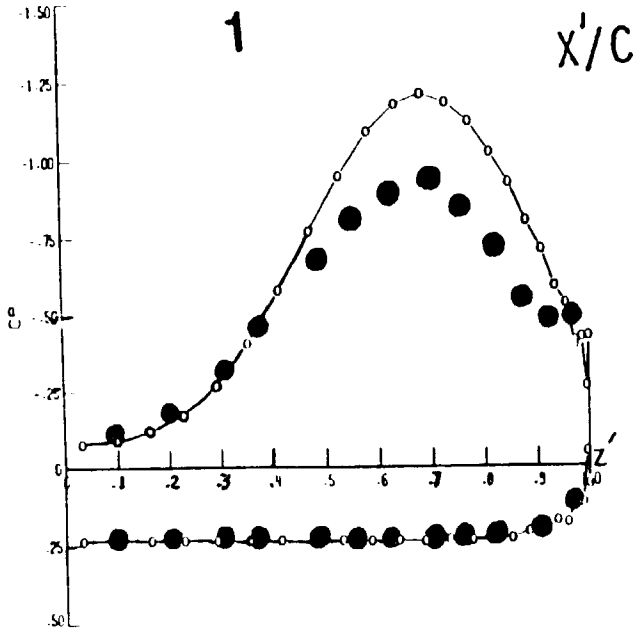

- Experiment[22], $X'/C = 0.8$ (averaged)
- Implicit Scheme–LD, $X'/C = 0.81$

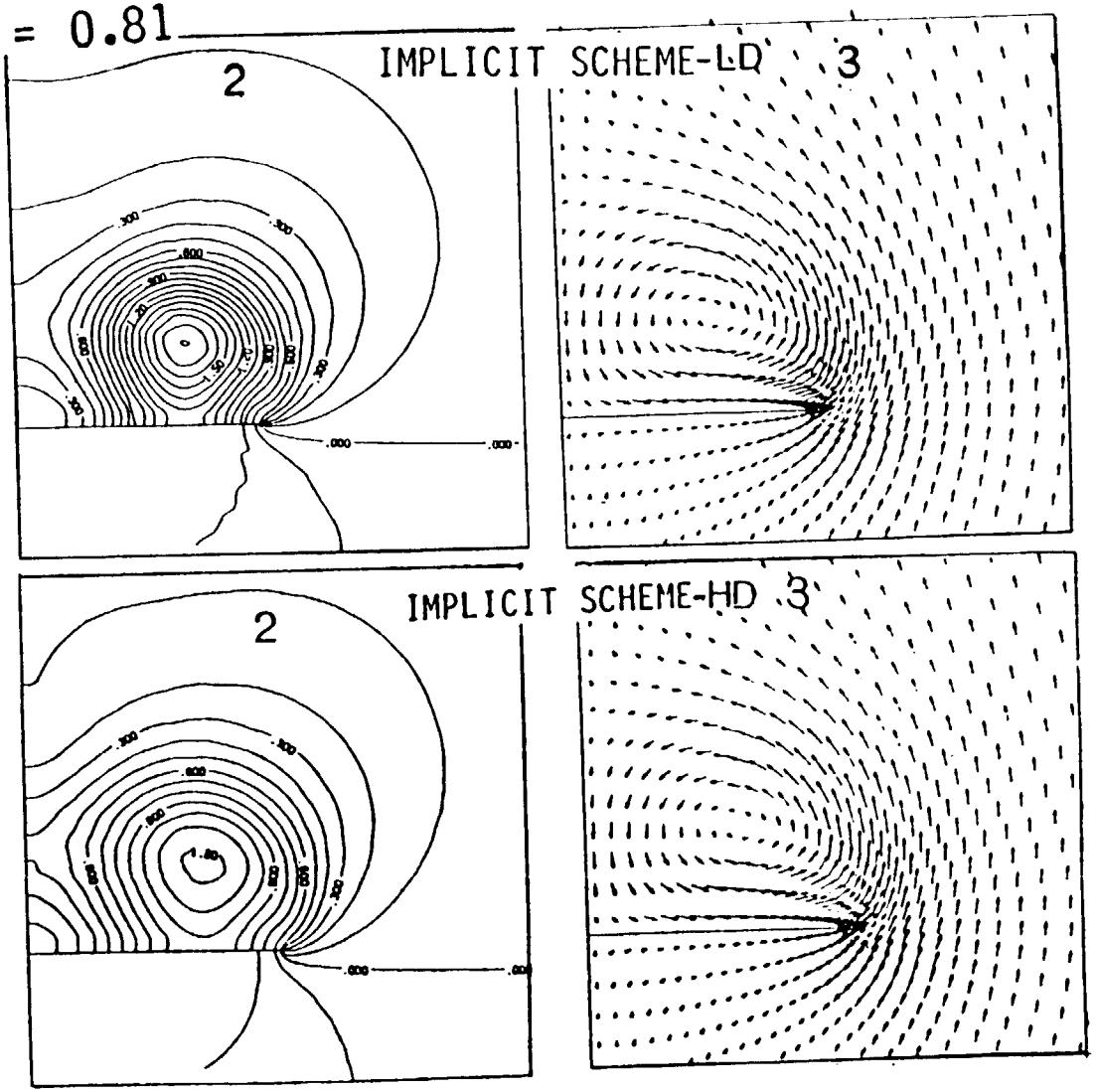

$X'/C = 1.02$

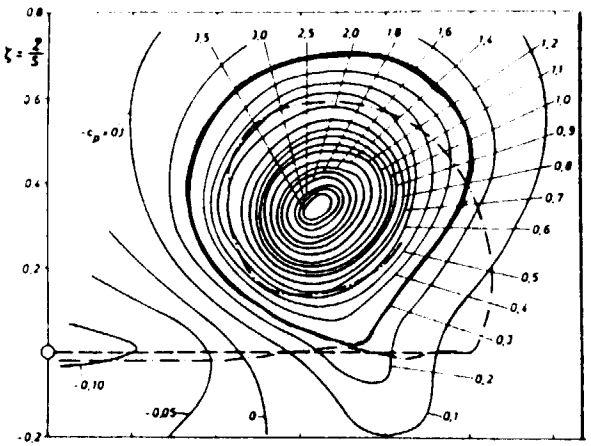

Experimental C_p-Contours[22]

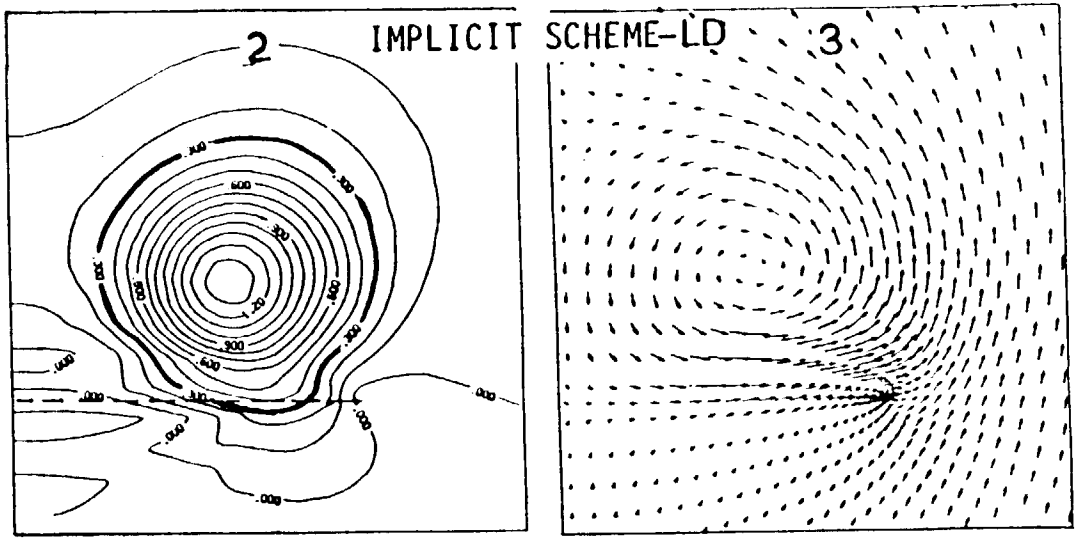

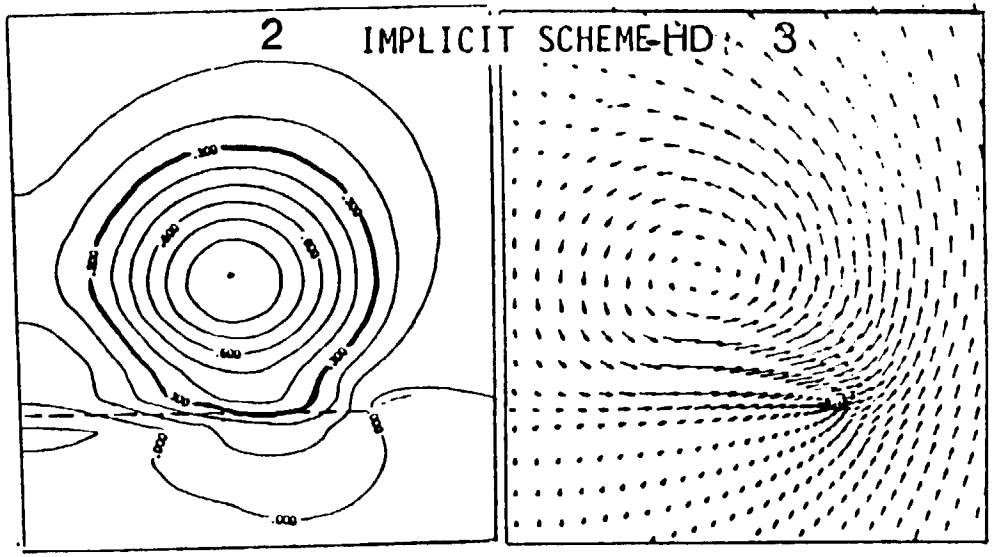

X'/C = 1.25

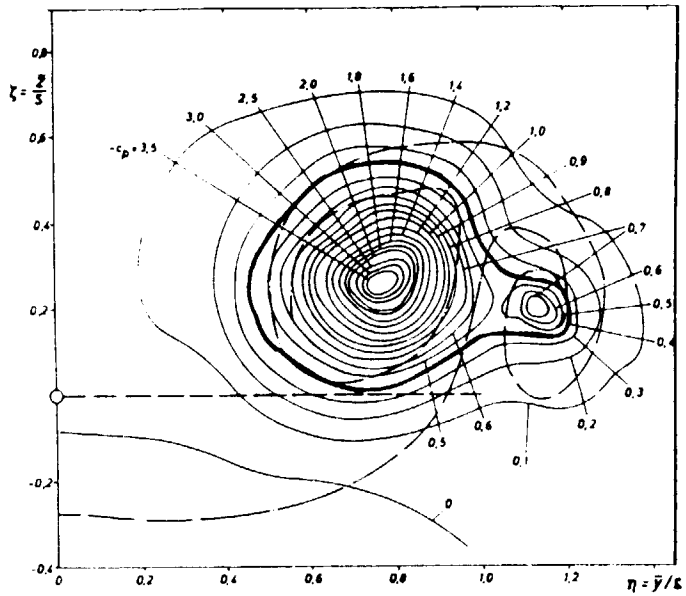

Experimental C_p-Contours[22]

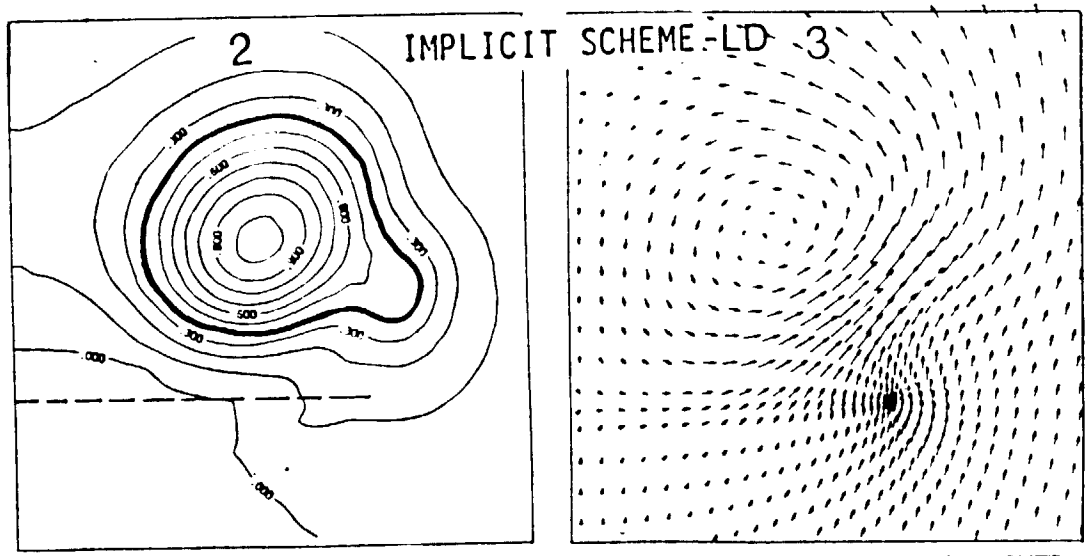

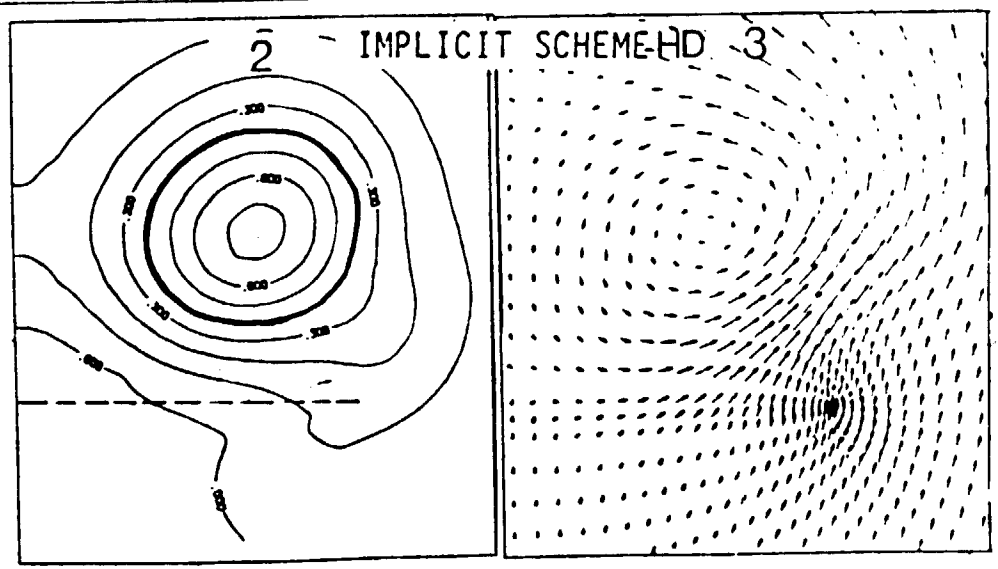

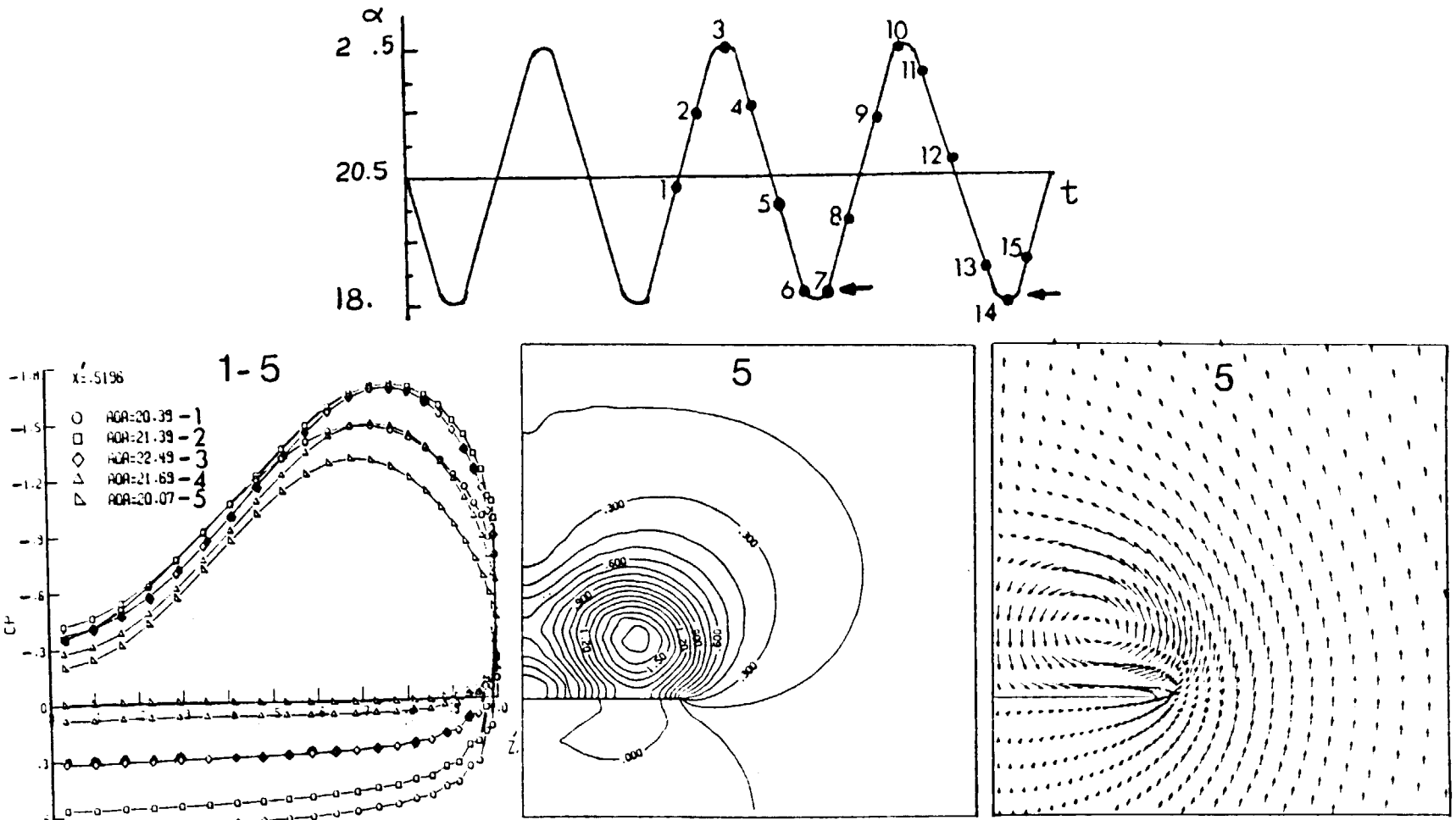

◆ AOA=22.5° (Ref. 25)

Fig. 5
(Continued)

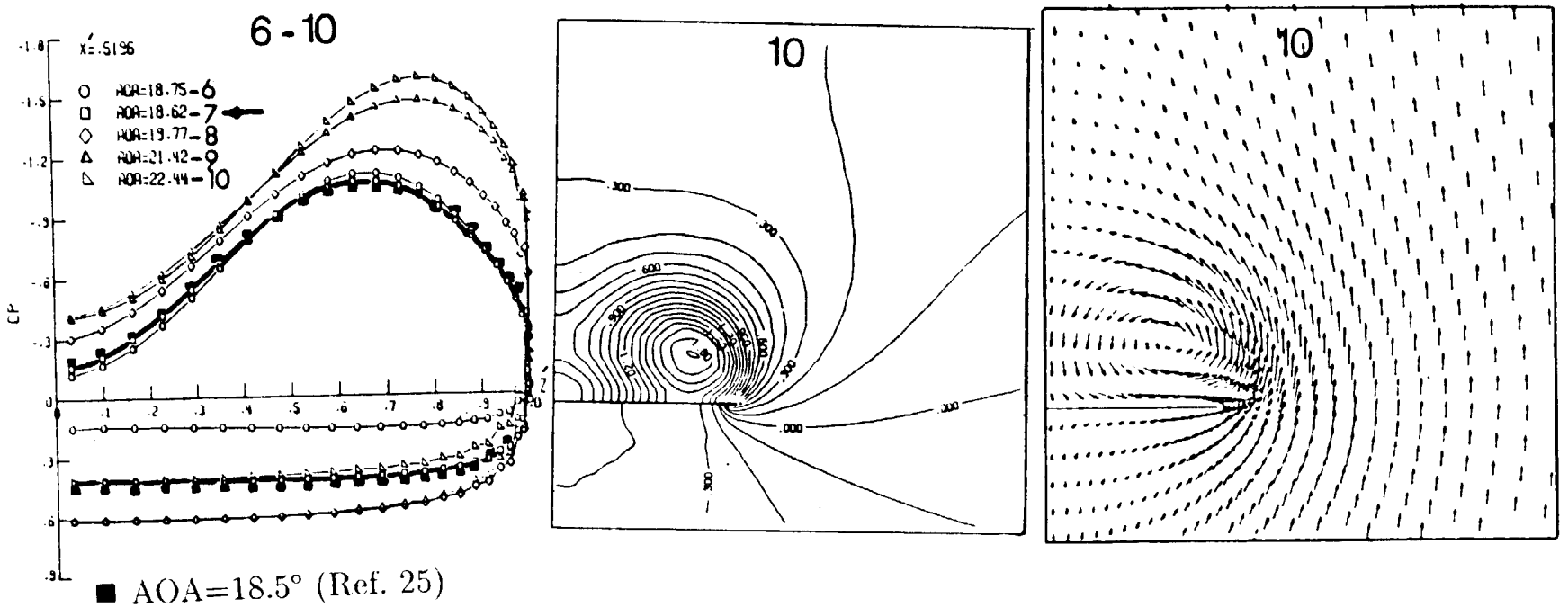

■ AOA=18.5° (Ref. 25)

Fig. 5
(Concluded)

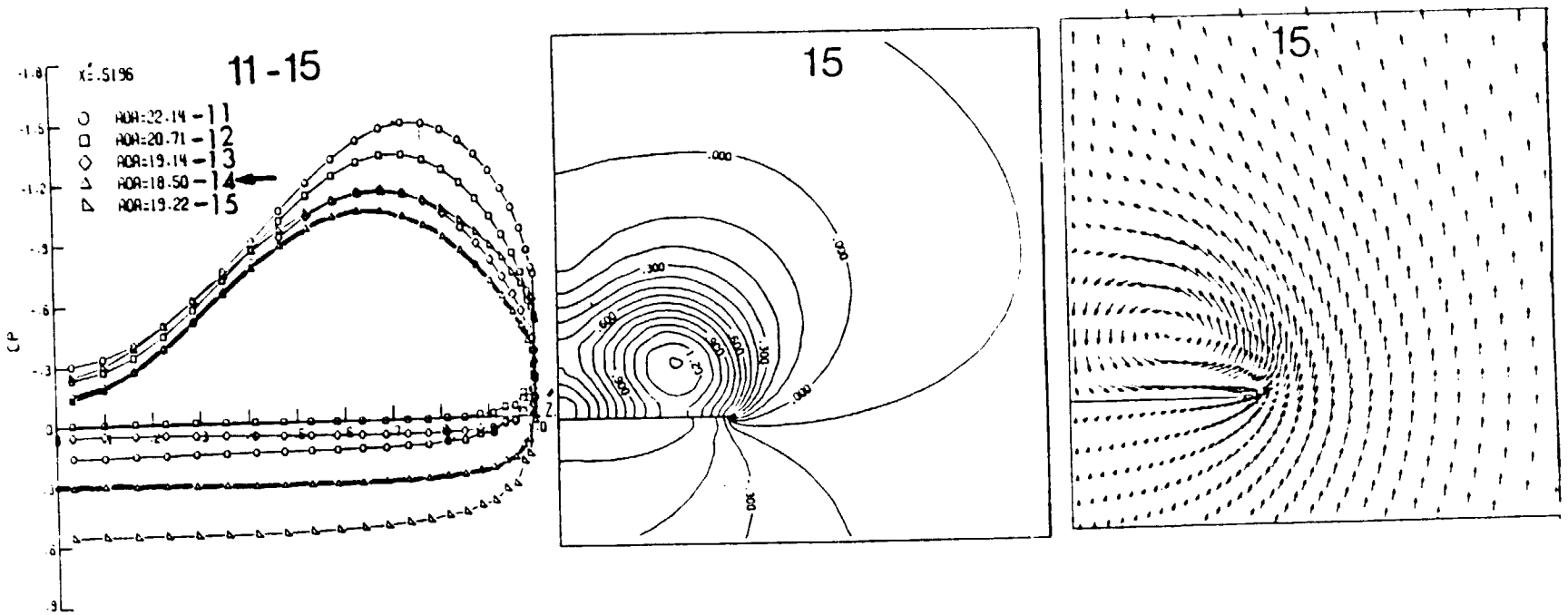

AIAA '89

AIAA 89-0553

Navier-Stokes Computations of Separated Vortical Flows past Prolate Spheroid at Incidence

T. C. Wong and O. A. Kandil
Old Dominion University
Norfolk, Virginia 23529-0247

C. H. Liu
NASA Langley Research Center
Hampton, Virginia 23665

27th Aerospace Sciences Meeting
January 9–12, 1989/Reno, Nevada

NAVIER-STOKES COMPUTATIONS OF SEPARATED VORTICAL FLOWS PAST PROLATE SPHEROID AT INCIDENCE

Tin-Chee Wong* and Osama A. Kandil**
Old Dominion University, Norfolk, VA 23529-0247

C. H. Liu***
NASA Langley Research Center, Hampton, VA 23665

Abstract

The problem of steady incompressible viscous flow past prolate spheroids at incidence is formulated using the unsteady incompressible thin-layer Navier-Stokes (NS) equations and the unsteady compressible thin-layer Navier-Stokes equations. For the incompressible equations, a certain level of unsteady artificial compressibility is added to the continuity equation to secure the coupling with the momentum equations during the psuedo-time stepping. The two sets of Navier-Stokes equations are solved using a psuedo-time stepping of the implicit flux-difference splitting scheme on a curvilinear grid, which is generated by a transfinite grid generator. The Baldwin and Lomax algebraic eddy viscosity model is used to model the turbulent flow. The computational applications cover a 6:1 prolate spheroid at different angles of attack and different Reynolds number. The results are compared with the experimental data.

Introduction

The flow about slender bodies over a wide range of angles of attack is characterized by the presence of large scale vortices on the leeward side of the body as a result of the surface flow separations. As the angle of attack changes from low to very high values, the three-dimensional boundary-layer flow changes from an attached and vortex-free flow to a separated and vortex-dominated flow. At moderate to high angles of attack, the flow separates on the leeward side of body forming two symmetric vortices, which in turn cause secondary and possible tertiary vortices. At higher angles of attack, asymmetric steady or unsteady vortex flow develops and unfavorable changes occur in the force and moment characteristics. For additional details, the reader is referred to a recent survey paper by Newsome and Kandil[1], which covers the physical aspects and the numerical simulation of vortical flows past slender bodies and highly swept wings over a wide range of angle of attack and Mach number.

The present problem has been considered computationally[2-13] and experimentally[14-17] by several investigators due to its significance to aircraft and missiles applications. In particular, the problem of incompressible flow past prolate spheroids over a wide range of angles of attack has been considered for computational simulation by several investigators[2,4,6-8,10-12] due to the existence of detailed experimental data[14-17]. Three-dimensional integral boundary-layer equations have been used by Stock[2] and Tai[6] to solve for the flow around slender porlate spheroids at incidence. Ragab[4] has used the three-dimensional incompressible boundary-layer equations on a non-orthogonal coordinate system to solve for laminar, transitional and turbulent flows past a 6:1 ellipsoid of revolution at various incidences. In a recent paper, Ragab[8] coupled the boundary-layer equations with an inhomogeneous form of Euler equations to effect a mechanism of vorticity generation. The method was applied to the turbulent flow past a 6:1 prolate spheroid at incidence. Boundary layer-equations have also been used by Yanta and Wardlaw[3], Jettmar and Kordulla[5] and Patel and Break[7].

Newsome and Adams[9] used the MacCormack's explicit scheme to solve for the vortical flow over elliptical body missile using the unsteady compressible thin-layer Navier-Stokes equations. No skin-friction coefficient calculation or comparison was shown. Hartwich and Hall[13] solved for the vortical flow over a tangent-ogive cylinder using an implicit flux-difference splitting scheme for the unsteady incompressible thin-layer Navier-Stokes equations. The computer program used is called "VOR3DI" -- the same program we used in the present paper for the incompressible Navier-Stokes equations. Again, no skin friction calculation or comparison was shown in their paper.

Pan and Pulliam[10] used the implicit factorization scheme to solve the compressible thin-layer Reynolds-averaged Navier-Stokes equations for the incompressible flow over a 6:1-prolate spheroid at 10° angle of attack, 0.029 Mach number and 1.6×10^6 Reynolds number based on the ellipsoid length. The results were compared with the experimental data of Meier, et. al[15,17] and the sting-support of the body in the experiments was not modeled in the computational simulation. Moreover, geometrical singular lines were present along the body axis due to the grid used. The computations covered a laminar flow and a turbulent flow triggered at a quarter of the body length from the body nose where Baldwin and Lomax algebraic eddy viscosity model was used.

---

*Graduate Research Assistant, Department of Mechanical Engineering and Mechanics, Member AIAA.

**Professor, Department of Mechanical Engineering and Mechanics, Associate Fellow AIAA.

***Group Leader, Analytical Methods Branch, Senior Member AIAA.

$$\bar{G}_v = \frac{M_\infty \mu}{R_e \cdot J} [0, \Phi_1 u_\zeta + \Phi_2 \zeta_x, \Phi_1 v_\zeta + \Phi_2 \zeta_y, \Phi_1 w_\zeta + \Phi_2 \zeta_z, \Phi_1 [\frac{1}{2}(u^2 + v^2 + w^2)_\zeta + \frac{1}{P_r(\gamma-1)}(a^2)_\zeta] + \Phi_2 W]^t \quad (11)$$

In Eqs. (8)-(10), the pressure is related to the total energy per unit mass, e, the kinetic energy per unit mass and the density by the ideal gas equation

$$p = (\gamma-1)\rho [e - \frac{1}{2}(u^2 + v^2 + w^2)] \quad (12)$$

In Eqs. (2)-(11), the contravariant components of the velocity; U, V, W, the metric functions Φ_1 and Φ_2 and the Jacobian of transformation, J, are given by

$$U = \xi_x u + \xi_y v + \xi_z w \quad (13)$$

$$V = \eta_x u + \eta_y v + \eta_z w \quad (14)$$

$$W = \zeta_x u + \zeta_y v + \zeta_z w \quad (15)$$

$$\Phi_1 = \zeta_x^2 + \zeta_y^2 + \zeta_z^2 \quad (16)$$

$$\Phi_2 = (\zeta_x u_\zeta + \zeta_y v_\zeta + \zeta_z w_\zeta)/3 \quad (17)$$

$$J^{-1} = x_\xi (y_\eta z_\zeta - y_\zeta z_\eta) + x_\eta (y_\zeta z_\xi - y_\xi z_\zeta) + x_\zeta (y_\xi z_\eta - y_\eta z_\xi) \quad (18)$$

In Eqs. (2)-(5), a certain level of aritificial compressibility is added to the continuity equation through the time dependent term $\frac{\partial}{\partial t}(p/\beta)$ with constant β. The purpose of this term is to re-couple the continuity equation with the momentum equation producing a parabolic set of partial differential equations in time during the psuedo-time marching. Once steady flow solution is reached, the artificial compressibility term disappars. The incompressible equations are nondimensionalized using the reference parameters of L, V_∞, L/V_∞, ρ_∞ and μ_∞ for the length, velocity, time, density and molecular viscosity, respectively. For the compressible equations, the reference parameters are L, a_∞, L/a_∞, ρ_∞ and μ_∞ for the length, velocity, time, density and molecular viscosity, respectively. For the two sets of equations, the Reynolds number is defined as $R_e = \rho_\infty V_\infty \ell/\mu_\infty$.

Turbulence Modeling:

For turbulent modeling, the Navier-Stokes equations are transformed to the Reynolds-averaged equations by replacing the coefficient of molecular viscosity, μ, and the coefficient of thermal conductivity (in the case of compressible Navier-Stokes equations) k with

$$\mu_e = \mu + \mu_t = \mu(1 + \mu_t/\mu) \quad (19)$$

$$k_e = k + k_t = \frac{\mu C_p}{P_r}(1 + \frac{\mu_t}{\mu}\frac{P_r}{P_{r_t}}) \quad (20)$$

where μ_e is the effective viscosity, k_e the effective thermal conductivity, μ_t the turbulent viscosity, P_r the laminar Prandtl number, P_{rt} the turbulent Prandtl number and C_p the specific heat under constant pressure. The turbulent viscosity μ_t is obtained by using the two-layer algebraic eddy viscosity model which was first developed by Cebeci[19] for the boundary-layer equations and modified later by Baldwin and Lomax[20] for the Navier-Stokes equations. The turbulent viscosity in this model is given by

$$\mu_t = \begin{cases} (\mu_t)_i & r \le r_c \\ (\mu_t)_o & r_c > r \end{cases} \quad (21)$$

where r is the normal distance from the body surface (for the prolate spheroid it is in the direction of a ray from the axis) and r_c the smallest value of r at which the inner-layer turbulent viscosity $(\mu_t)_i$ is equal to the outer-layer turbulent viscosity $(\mu_t)_o$. For the inner layer, the turbulent viscosity is calculated by using the Van Driest algebraic formula

$$(\mu_t)_i = \rho \ell^2 |\omega| \quad (22)$$

where the mixing length ℓ is given by

$$\ell = k r [1 - \exp(-r^+/A^+)] \quad (23)$$

where k is the von Kármán constant, A^+ is a damping constant and r^+ is given by

$$r^+ = r (\rho_w \tau_w)^{1/2}/\mu_w \quad (24)$$

The subscript w refers to the body surface. In Eq. (22), $|\omega|$ is modulus of vorticity which is given by

$$|\omega| = |\nabla \times \bar{V}| = [(u_y - v_x)^2 + (v_z - w_y)^2 + (w_x - u_z)^2]^{1/2} \quad (25)$$

$$\delta_i = [(\ )_{i+1/2} - (\ )_{i-1/2}]/\Delta\xi \qquad (35)$$

and δ_j and δ_k are defined similarly. The inviscid fluxes E^n, F^n and G^n at the interfaces $i \mp 1/2$, $j \mp 1/2$ and $k \mp 1/2$ separate the negative and positive waves and hence they can be written as the solution to a Riemann problem in the form

$$E^n_{i+1/2} = E^n_i + (\Delta E^-_{i+1/2})^n = E^n_{i+1} - (\Delta E^+_{i+1/2})^n \qquad (36)$$

Similar expressions are used for $E^n_{i-1/2}$, $F^n_{j\pm1/2}$ and $G^n_{k\pm1/2}$. Following Roe's scheme, we rewrite $(\Delta E^{\mp}_{i\pm1/2})^n$ [similarly for $(\Delta F^{\mp}_{j\pm1/2})^n$ and $(\Delta G^{\mp}_{k\pm1/2})^n$] as

$$(\Delta E^{\mp}_{i\pm1/2})^n = \pm\,(A^{\mp}_{i\pm1/2})^n\,\delta_{i\pm1/2}\,Q^n \qquad (37)$$

$$(A^+_{i+1/2})^n = A^{+n}\left(\frac{Q^n_i + Q^n_{i+1}}{2}\right) \qquad (38)$$

Using a similarity transformation, the matrices A, B and C are split. For matrix A, the splitting is given by

$$A = R\,\Lambda\,L = R\,[\Lambda^+ - \Lambda^-]\,L = A^+ - A^- \qquad (39)$$

where $\Lambda^{\pm} = (\Lambda \pm |\Lambda|)/2$ are diagonal matrices of eigenvalues, R and L are the right and left eigenvector matrices of A. Using Eqs. (35) - (39) into Eq. (34), we obtain

$$\begin{aligned}
&[I/J_{i,j,k}\,\Delta t) + (A^+_{i-1/2}\,\delta_{i-1/2} \\
&- A^-_{i+1/2}\,\delta_{i+1/2}) + (B^+_{j-1/2}\,\delta_{j-1/2} \\
&- B^-_{i+1/2}\,\delta_{i+1/2}) + (C^+_{k-1/2}\,\delta_{k-1/2} \\
&- C^-_{k+1/2}\,\delta_{k+1/2})]^n\,\Delta Q^n = -[(A^+_{i-1/2}\,\delta_{i-1/2} \\
&- A^-_{i+1/2}\,\delta_{i+1/2}) + (B^+_{j-1/2}\,\delta_{j-1/2} \\
&- B^-_{j+1/2}\,\delta_{j+1/2}) + (C^+_{k-1/2}\,\delta_{k-1/2} \\
&- C^-_{k+1/2}\,\delta_{k+1/2})]^n\,Q^n
\end{aligned} \qquad (40)$$

Since the scheme of Eq. (40) is highly dissipative, a high resolution scheme is used to enhance the scheme accuracy. For one-dimensional equation of Eq. (40), the high resolution scheme gives

$$\begin{aligned}
&[I/(J_{i,j,k}\,\Delta t) + (A^+_{i-1/2}\,\delta_{i-1/2} \\
&- A^-_{i+1/2}\,\delta_{i+1/2})]^n\,\Delta Q^n \\
&= (R_{i+1/2}\,\Lambda^-_{i+1/2}\,[I - 0.5\,(\Phi^-_{i+1} \\
&- \Phi^+_i)]\,L_{i+1/2})^n\,\delta_{i+1/2}\,Q^n \\
&- (R_{i-1/2}\,\Lambda^+_{i-1/2}\,[I + 0.5\,(\Phi^-_i \\
&- \Phi^+_{i-1})]\,L_{i-1/2})^n\,\delta_{i-1/2}\,Q^n
\end{aligned} \qquad (41)$$

where

$$\Phi^{\pm}_i = \mathrm{diag}\,(\phi^{\pm}_1, \phi^{\pm}_2, \phi^{\pm}_3, \phi^{\pm}_4)_i \qquad (42\text{-a})$$

and

$$\phi^{\pm}_{m,i} \equiv \text{TVD limiters} = \mathrm{Max}\,[0, \min (1, r^{\pm}_{m,i}, 2r^{\mp}_{m,i\pm1})] \qquad (42\text{-b})$$

$$r^{\pm}_{m,i} = \begin{cases} \left(\dfrac{\delta_{i-1/2}\,w^n_m}{\delta_{i+1/2}\,w^n_m}\right)\pm1 & \text{for } \delta_{i\pm1/2}\,w^n_m \neq 0 \\ 0 & \text{for } \delta_{i\pm1/2}\,w^n_m = 0 \end{cases} \qquad (42\text{-c})$$

where

$$w = LQ \qquad (42\text{-d})$$

The viscous flux G_v is centrally differenced. Thus, for the thin-layer Navier-Stokes equations, the difference equations becomes

$$\begin{aligned}
&[I/(J_{i,j,k}\,\Delta t) + A^+_{i-1/2}\,\delta_{i-1/2} - A^-_{i+1/2}\,\delta_{i+1/2} \\
&+ B^+_{j-1/2}\,\delta_{j-1/2} - B^-_{j+1/2}\,\delta_{j+1/2} \\
&+ (C^+ + Z)_{k-1/2}\,\delta_{k-1/2} \\
&- (C^- + Z)_{k+1/2}\,\delta_{k+1/2}]^n\,\Delta Q^n = -\,\mathrm{RES}\,(Q^n)
\end{aligned} \qquad (43)$$

where Z is the Jacobian matrix corresponding to the viscous flux G_v, and RES (Q^n) is the discrete representation of the spatial derivatives in Eq. (1), evaluated at n with the high resolution scheme applied to the inviscid fluxes. Equation (43) is solved by using a symmetric, planar Gauss-Seidel relaxation in the ξ-direction and approximate factorization in the η and ζ directions. This factors Eqs (43) in the form

windward angle range θ = 0 - 50°. This is attributed to the fully turbulent flow assumption of the computations while in the experimental case the flow is laminar to transional. Beyond this angle, the CFL3D results are in excellent agreement with the experimental data. The results of the VOR3DI are unacceptable. Finally, we show a comparison of the surface pressure and skin friction coefficient in the axial vertical plane. The C_p results of the two codes are close while the C_f results are substantially different.

The CFL3D code took 3000 time steps to reduce the residual error by four orders of magnitude while the VOR3DI code took 400 time steps to reduce the residual error by two orders of magnitude.

2. Fixed Transitional Flow (X/L = 0.2), Re = 7.7×10^6, α = 10°:

Here, the turbulent model is turned on at the axial location X/L = 0.2. Figures 10-14 fully cover this case. In Fig. 10, we show the cross-flow velocity vectors in the cross-flow planes which are computed by the CFL3D. It is seen that the flow separation is very small in the forward planes, while in the rearward planes it grows larger. Figure 11 shows a comparison of the computed surface pressure by CFL3D and VOR3DI in the same three cross-flow planes. The results are in good agreement. In Fig. 12, the corresponding computed skin-friction coefficient by CFL3DI and VOR3DI along with the experimental data are presented. Again CFL3D results are in good agreement with the experimental data while those of the VOR3DI show substantial discrepancies in the windward side.

Figure 13 shows a comparison of the computed surface pressure and skin friction in the axial plane. While the computed surface pressure of CFL3D and VOR3DI are in good agreement, the computed skin friction coefficient show substantial differences.

Figure 14 shows a comparison of the convergence history of CFL3D and VOR3DI. It is seen that the CFL3D takes 6000 time steps to reduce the residual error by four orders of magnitude (which is twice the number of time steps needed for the turbulent flow case). The VOR3DI still takes 400 time steps to reduce the residual error by two orders of magnitude.

3. Laminar Flow Case, Re = 1.6×10^6, α =10°:

The results of this case is covered in Figs. 15-17. Here, we only consider the results of CFL3D which are shown after 10,000 time steps. In Fig. 15, we show a comparison of the computed skin-friction coefficient with those of the experimental data at six cross-flow planes. It is seen that the results are in good agreement with the experimental data in the θ range of 0° - 150 in the forward part of the body and in the θ range of 0 - 115° in the rear part of the body. In the remainder range of of θ, the computed results are substantially different from the experimental data. This is attributed to the flow transition from laminar to turbulent in the region of separated flow, which has not been accounted for in the computational simulation. It should be pointed out here that the skin-friction results of this case obtained here in this paper, after 10,000 iterations, are a little different from those obtained by the same code in Ref. 11, where 6,000 iterations have been used. It is obvious from Fig. 17 that the residual error is still coverging at the 10,000 iteration step after it showed constant residual error in the range of 5,000-6,000 iterations. Figure 16 shows good agreement of the surface pressure in the axial vertical plane with that of experimental data. The computed skin friction in the leeward side shows substantial difference with the experimental data.

Concluding Remarks

The problem of steady incompressible viscous flow past a 6:1-prolate spheroid at incidence has been solved using two sets of the Navier-Stokes equations; an incompressible set and a compressible set. The computational scheme used for the two sets is the implicit flux-difference splitting scheme. The incompressible set is solved using a computer code known as "VOR3DI" and the compressible set is solved using a computer code known as "CFL3D". The compressible code has been applied to three test cases; a fully turbulent flow case, a fixed transition flow case and a laminar flow case, while the incompressible code has been applied to the first two cases. The predicted results of the compressible code are in good agreement with the experimental data while those of the incompressible code are unacceptable with the exception of the surface pressure. For the high-angle-of-attack turbulent flow case, the incompressible code predicts small primary and secondary vortices which are closer to the body with larger azimuthal angles than those of the experimental data.

The compressible code, however, takes large number of time steps to converge. The number of time steps are inversely proportional to the Reynolds number. On the other hand, the incompressible code takes small number of time steps to converge. Additional work is needed to modify the incompressible flow code for better prediction of the viscous effects; e.g., skin-friction coefficient, details of the primary vortex core and the secondary vortex. Perhaps one should switch the upwind flux-difference splitting scheme to central differencing as the residual drops down to order of 10^{-2}, since the incompressible equations then are dominantly elliptic. Obviously, one also need better transitional and turbulent models for this problem than the simple minded approach of switching on the turbulent model at a prescribed position. It should be also recalled that some of the constants of the two-layer, algebraic model of Balwin and Lomax have been obtained from matching its results with transonic flow results -- a point which needs further investigation.

Acknowledgement

This research work has been supported by NASA Langley Research Center under grant number NAS1-18584-08. The authors would like to thank Dr. J. L. Thomas for providing a copy of the

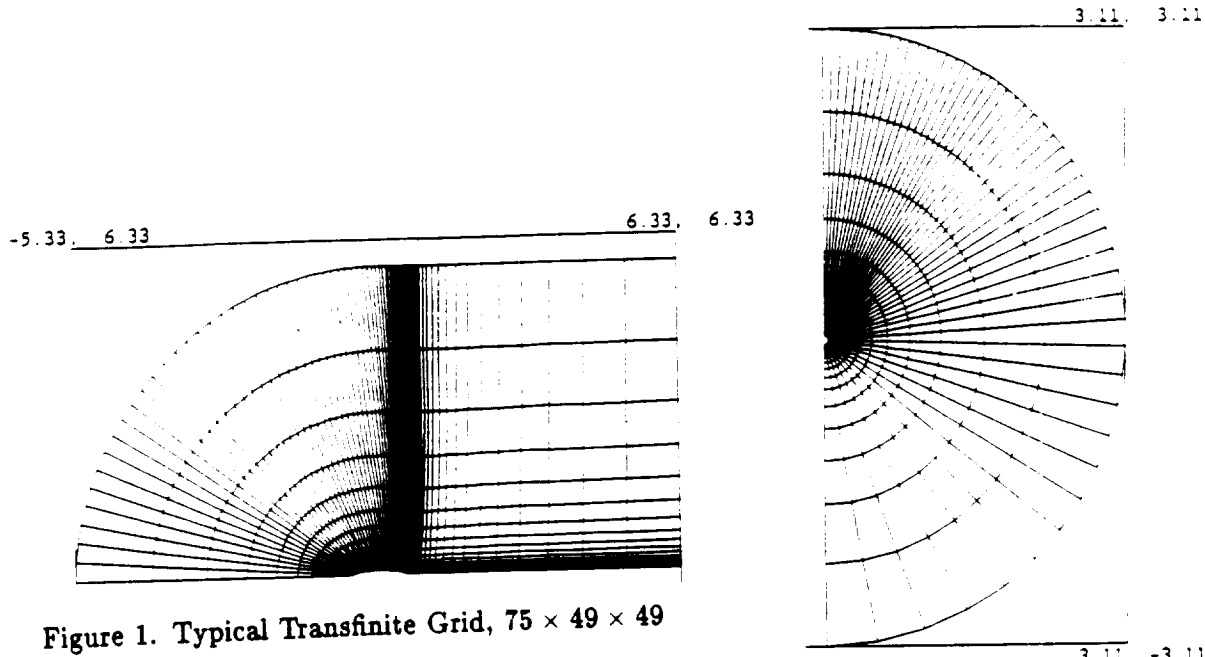

Figure 1. Typical Transfinite Grid, 75 × 49 × 49

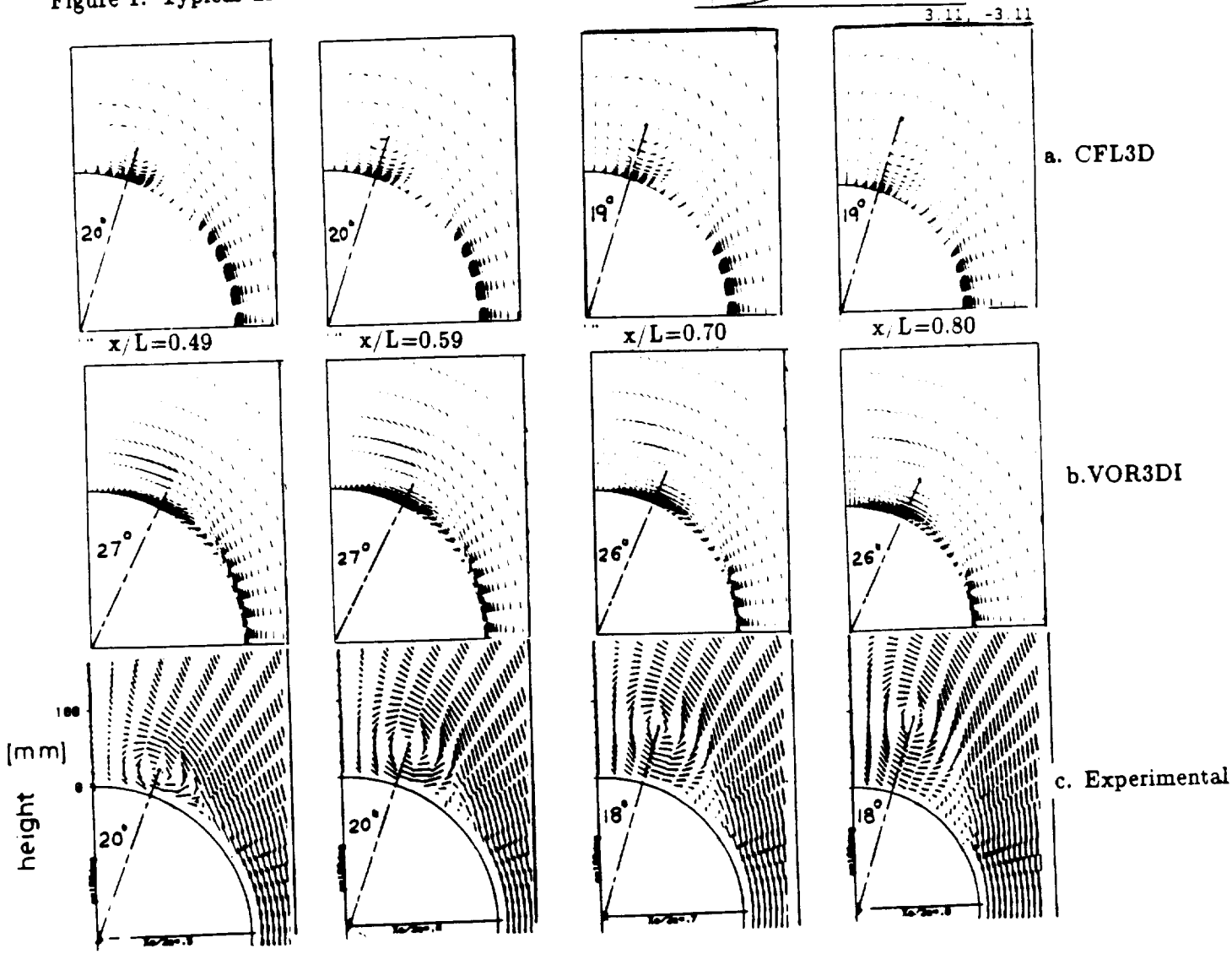

Figure 2. Cross-Flow Velocity Vectors, α=30.0, Re=7,200,000

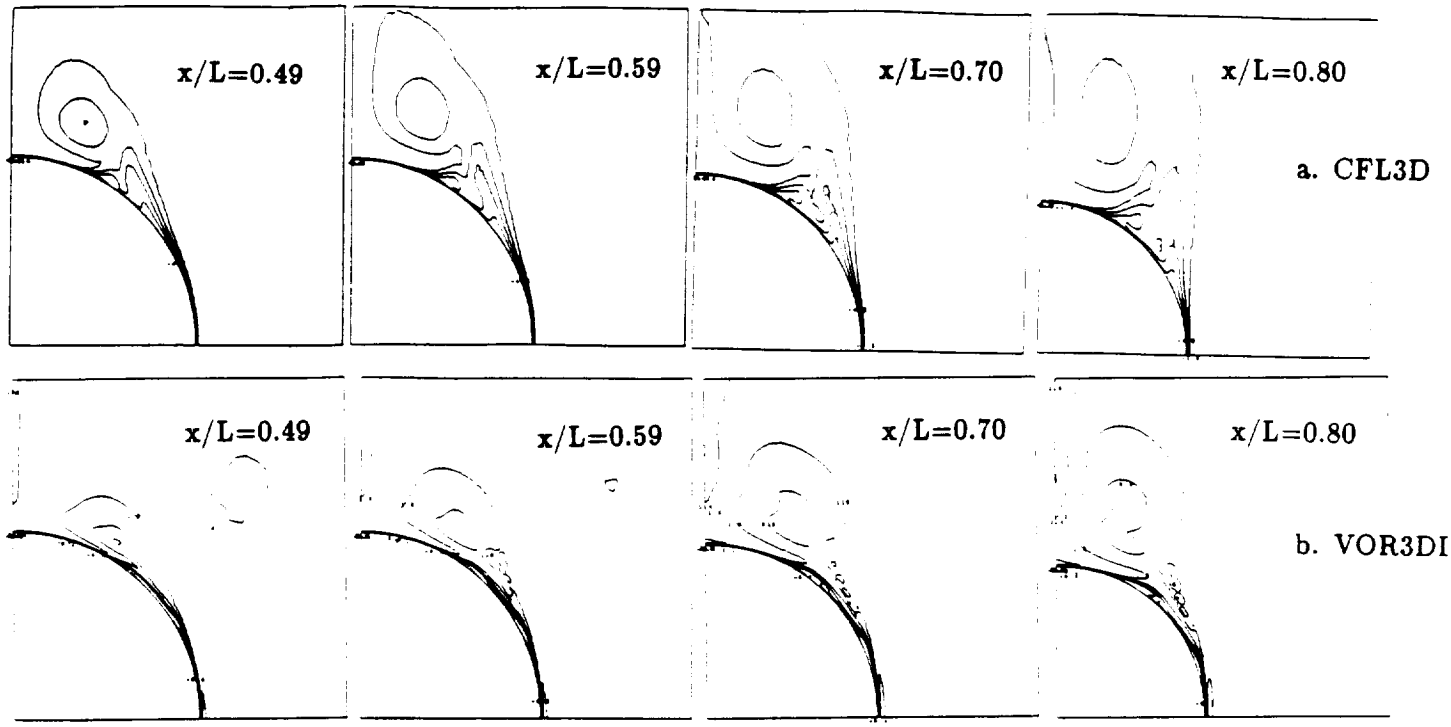

Figure 6. Total Pressure Contour, α=30.0, Re=7,200,000

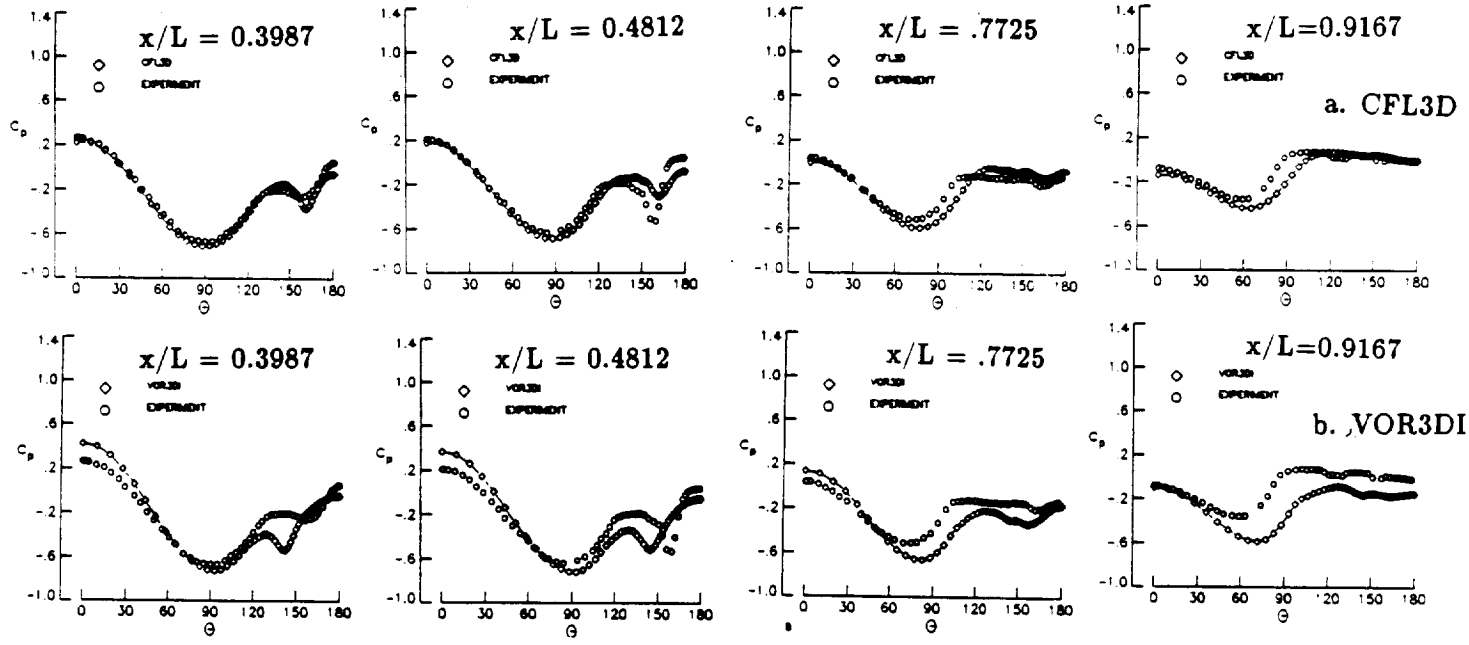

Figure 7. Surface Pressure in Cross-Flow Planes, α=30.0, Re=7,200,000

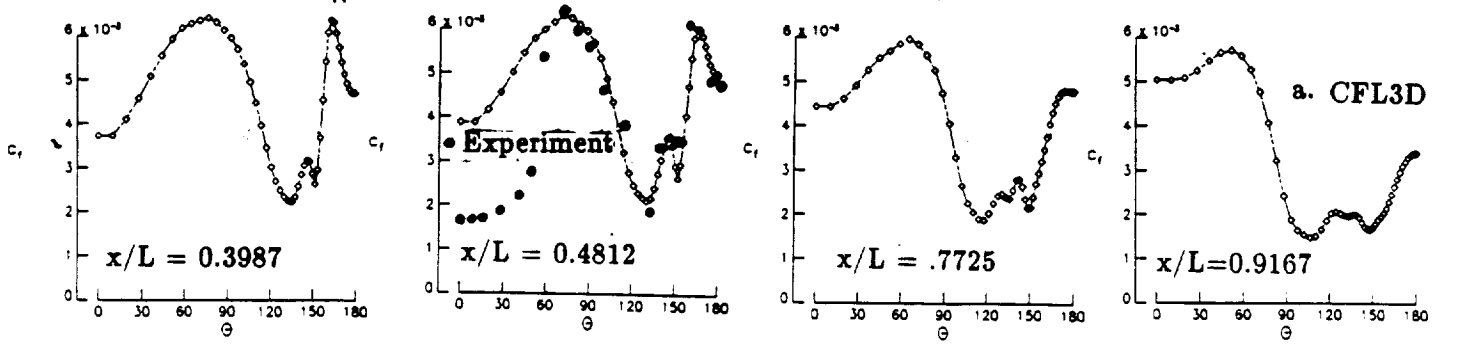

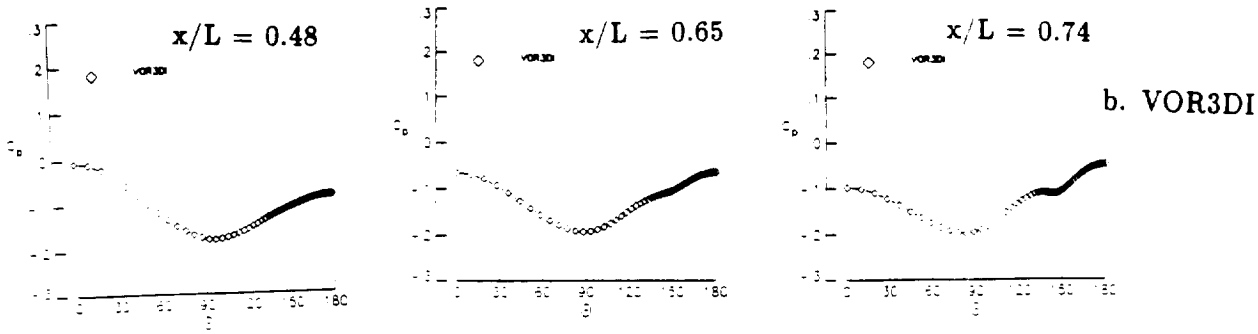

Figure 11. Surface Pressure in Cross-Flow Planes, α=10.0, Re=7,700,000, (0.2 Fixed Transition)

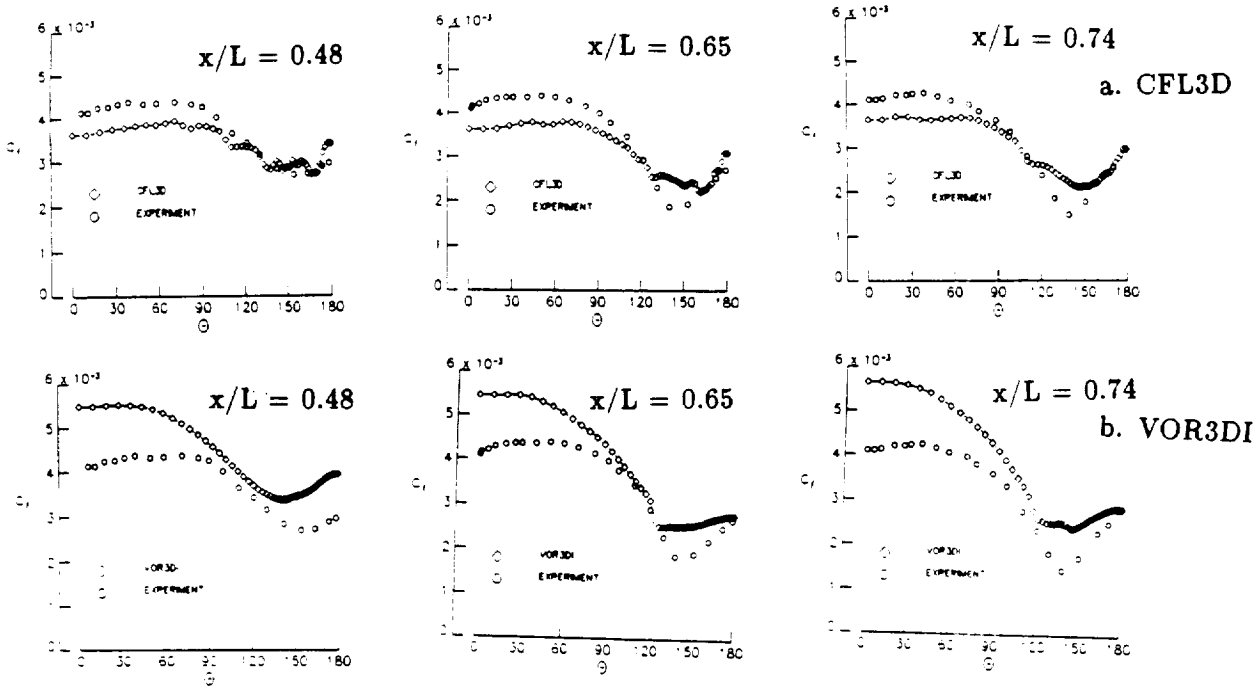

Figure 12. Skin-Friction Coefficient in Cross-Flow Planes, α=10.0, Re=7,700,000 (0.2 Fixed Transition)

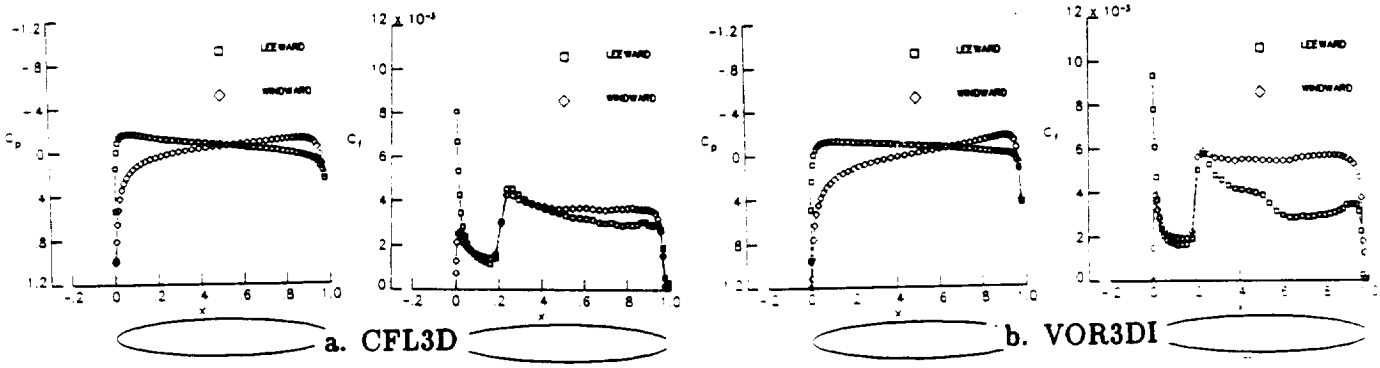

Figure 13. Surface-Pressure and Skin-Friction Coefficients in the Axial Vertical Plane, α=10.0, Re=7,200,000 (0.2 Fixed Transition)